



**NEAR EAST UNIVERSITY  
INSTITUTE OF GRADUATE STUDIES  
DEPARTMENT OF COMPUTER ENGINEERING**

**BRAIN TUMOR SEGMENTATION USING NON-PARAMETRIC  
LOCALIZATION AND  
ENHANCEMENT METHODS WITH U-NET**

**Ph.D. THESIS**

**Ahmet İLHAN**

**Nicosia  
February, 2022**

**AHMET İLHAN**

**BRAIN TUMOR SEGMENTATION USING  
NON-PARAMETRIC LOCALIZATION AND  
ENHANCEMENT METHODS WITH U-NET**

**Ph.D. THESIS**

**2022**



**NEAR EAST UNIVERSITY  
INSTITUTE OF GRADUATE STUDIES  
DEPARTMENT OF COMPUTER ENGINEERING**

**BRAIN TUMOR SEGMENTATION USING NON-PARAMETRIC  
LOCALIZATION AND  
ENHANCEMENT METHODS WITH U-NET**

**Ph.D. THESIS**

**Ahmet İLHAN**

**Supervisors**

**Prof. Dr. Rahib ABİYEV**

**Assoc. Prof. Dr. Boran ŞEKEROĞLU**

**Nicosia**

**February, 2022**

## Approval

We certify that we have read the thesis submitted by Ahmet İLHAN titled “**Brain Tumor Segmentation using Non-Parametric Localization and Enhancement Methods with U-Net**” and that in our combined opinion it is fully adequate, in scope and in quality, as a thesis for the degree of Doctor of Philosophy in Computer Engineering.

Examining Committee	Name-Surname	Signature
Head of the Committee:	Assoc. Prof. Dr. Eser GEMİKONAKLI	.....
Committee Member:	Assoc. Prof. Dr. Kamil DİMİLİLER	.....
Committee Member:	Assoc. Prof. Dr. Mary AGOYI	.....
Committee Member:	Assist. Prof. Dr. Elbrus İMANOV	.....
Supervisor:	Prof. Dr. Rahib ABİYEYEV	.....
Co-Supervisor:	Assoc. Prof. Dr. Boran ŞEKEROĞLU	.....

Approved by the Head of the Department

...../...../20...

Prof. Dr. Rahib ABİYEYEV  
Head of the Department

Approved by the Institute of Graduate Studies

...../...../20...

Prof. Dr. Kemal Hüsnü Can BAŞER  
Head of the Institute

## **Declaration**

I hereby declare that all information, documents, analysis and results in this thesis have been collected and presented according to the academic rules and ethical guidelines of Institute of Graduate Studies, Near East University. I also declare that as required by these rules and conduct, I have fully cited and referenced information and data that are not original to this study.

Ahmet İLHAN

30/01/2022

## Acknowledgments

I would first like to thank my supervisor Prof. Dr. Rahib Abiyev for his guidance, encouragement, and patience. I would also like to thank my co-supervisor Assoc. Prof. Dr. Boran Şekeroğlu for his support, effort and guidance he gave me all throughout my studies for this thesis.

I am also thankful to my university in general and my department in particular for providing me with the necessary equipment to realize the test runs of my software that needed enough processing power.

Finally, I thank my family for their patience, constant support, and inspiration. Without them, completing this thesis would have been impossible.

Ahmet İLHAN

**Abstract****Brain Tumor Segmentation using Non-Parametric Localization and Enhancement Methods with U-Net****İlhan, Ahmet****Ph.D., Department of Computer Engineering****February, 2022, 54 pages**

Segmentation is one of the most critical steps in analyzing medical images since it provides meaningful information for diagnosing, monitoring, and treating brain tumors. Several artificial intelligence-based systems have been developed to perform this task accurately in recent years. However, some tumors' unobtrusive or low-contrast occurrence and similarities to healthy brain tissues make the segmentation task challenging. These yielded researchers to develop new methods for preprocessing the images and improving their segmentation abilities. This study proposes an efficient system for the segmentation of the complete brain tumors from MRI images based on non-parametric tumor localization and enhancement methods with a deep learning architecture named U-Net. Initially, the histogram-based tumor localization method is applied to localize the tumorous regions. Then the tumor enhancement method is used to modify the localized regions to increase the visual appearance of indistinct or low-contrast tumorous regions. The resultant images are fed to the traditional U-Net architecture to segment the complete brain tumors. The performance of the proposed system is tested on benchmark datasets, BRATS 2012 (HGG-LGG), BRATS 2019, and BRATS 2020, and achieved superior results as 0.94, 0.85, 0.87, 0.88 dice scores, respectively. The results achieved by the proposed system and comparisons showed that the proposed tumor localization and enhancement methods improve the segmentation ability of the deep learning architectures and provide high-accuracy and low-cost segmentation of complete brain tumors in MRI images.

**Keywords:** Brain tumor, localization, enhancement, segmentation, U-Net

## Özet

### U-Net ile Parametrik Olmayan Lokalizasyon ve İyileştirme Yöntemleri Kullanılarak Beyin Tümörü Segmentasyonu

İlhan, Ahmet

Doktora, Bilgisayar Mühendisliği Bölümü

Şubat, 2022, 54 sayfa

Segmentasyon, beyin tümörlerinin teşhisi, takibi ve tedavisi için anlamlı bilgiler sağladığı için tıbbi görüntülerin analizinde en kritik adımlardan biridir. Son yıllarda bu görevi doğru bir şekilde yerine getirmek için çeşitli yapay zeka tabanlı sistemler geliştirilmiştir. Bununla birlikte, bazı tümörlerin göze batmayan veya düşük kontrastlı oluşumu ve sağlıklı beyin dokularına benzerlikleri, segmentasyon görevini zorlaştırır. Bunlar, araştırmacıların görüntüleri önceden işlemek ve segmentasyon yeteneklerini geliştirmek için yeni yöntemler geliştirmesini sağladı. Bu çalışma, U-Net adlı bir derin öğrenme mimarisi ile parametrik olmayan tümör lokalizasyon ve iyileştirme yöntemlerine dayanan MRI görüntülerinden tam beyin tümörlerinin segmentasyonu için verimli bir sistem önermektedir. İlk olarak, tümürlü bölgelerin lokalize edilmesi için histogram tabanlı tümör lokalizasyon yöntemi uygulanır. Daha sonra, belirgin olmayan veya düşük kontrastlı tümürlü bölgelerin görsel görünümünü artırmak için lokalize bölgeleri modifiye etmek için tümör iyileştirme yöntemi kullanılır. Ortaya çıkan görüntüler, tam beyin tümörlerini segmentlere ayırmak için geleneksel U-Net mimarisine beslenir. Önerilen sistemin performansı, BRATS 2012 (HGG-LGG), BRATS 2019 ve BRATS 2020 karşılaştırmalı veri setleri üzerinde test edilmiş ve sırasıyla 0.94, 0.85, 0.87, 0.88 zar puanları gibi üstün sonuçlar elde edilmiştir. Önerilen sistem ve karşılaştırmalar tarafından elde edilen sonuçlar, önerilen tümör lokalizasyon ve iyileştirme yöntemlerinin derin öğrenme mimarilerinin segmentasyon yeteneğini geliştirdiğini ve MRI görüntülerinde tam beyin tümörlerinin yüksek doğrulukta ve düşük maliyetli segmentasyonunu sağladığını gösterdi.

**Anahtar Kelimeler:** Beyin tümörü, lokalizasyon, iyileştirme, segmentasyon, U-Net



## Table of Contents

Approval.....	i
Declaration .....	ii
Acknowledgments .....	iii
Abstract .....	iv
Özet .....	v
Table of Contents .....	vi
List of Tables.....	ix
List of Figures .....	x
List of Abbreviations.....	xi

### CHAPTER I

Introduction .....	1
Background .....	1
Thesis Layout .....	3

### CHAPTER II

Literature Review .....	4
Systems Based on Traditional Methods.....	4
Combined Systems.....	6
CNN-Based Systems.....	7

### CHAPTER III

Digital Image Processing .....	11
Image Acquisition .....	11
Digital Image.....	12
Image Compression.....	14
Inter-Pixel Redundancy.....	14
Coding Redundancy .....	14
Psychovisual Redundancy.....	14
Compression Methods.....	15
Lossy Compression Technique .....	15
Lossless Compression Technique .....	15

Image Enhancement .....	15
Spatial Domain .....	15
Frequency Domain .....	16
Image Segmentation .....	16

#### CHAPTER IV

Deep Learning and Convolutional Neural Networks .....	18
Deep Learning .....	18
Convolutional Neural Networks .....	18
Convolution Operation .....	19
Convolutional Layer .....	19
Sparse Connectivity .....	20
Parameter Sharing .....	20
Pooling Layer .....	21
Fully Connected Layer .....	21
CNN Architectures for Image Segmentation .....	21
SegNet .....	21
U-Net .....	22

#### CHAPTER V

Methodology .....	24
Proposed System .....	24
Dataset .....	25
Mean Filter .....	26
Proposed Tumor Localization and Enhancement Methods .....	27
Evaluation Metrics .....	32

#### CHAPTER VI

Results and Discussions .....	34
Experimental Design .....	34
Results .....	35
Comparisons .....	38
Discussions .....	41

## CHAPTER VII

Conclusion .....	43
REFERENCES.....	44
APPENDICES .....	49
Appendix A: Ethical Approval Document.....	49
Appendix B: Curriculum Vitae .....	50
Appendix C: Similarity Report .....	53
Appendix D: Dataset Description .....	54

**List of Tables**

<b>Table 1.</b> Evaluation Results of the BRATS 2012 HGG Images.....	35
<b>Table 2.</b> Evaluation Results of the BRATS 2012 LGG Images .....	35
<b>Table 3.</b> Evaluation Results of the BRATS 2019 Dataset.....	36
<b>Table 4.</b> Evaluation Results of the BRATS 2020 Dataset.....	37
<b>Table 5.</b> Comparison Results of the Proposed System on BRATS 2012 Dataset....	38
<b>Table 6.</b> Comparison Results of the Proposed System on BRATS 2019 Dataset....	39
<b>Table 7.</b> Comparison Results of the Proposed System on BRATS 2020 Dataset....	39

## List of Figures

<b>Figure 1.</b> The Sampling and Quantization of Digital Images .....	11
<b>Figure 2.</b> Basic Structure of Digital Images .....	12
<b>Figure 3.</b> Sample Images for Each Digital Image Group .....	13
<b>Figure 4.</b> Pixelation on Digital Images .....	13
<b>Figure 5.</b> The Process for How a Segmentation Technique Works .....	17
<b>Figure 6.</b> Sample CNN Architecture .....	19
<b>Figure 7.</b> SegNet Architecture.....	22
<b>Figure 8.</b> U-Net Architecture .....	23
<b>Figure 9.</b> The Block Diagram of the Proposed System.....	24
<b>Figure 10.</b> Sample Images for Modalities .....	25
<b>Figure 11.</b> Samples for Distinct and Indistinct Tumorous Images.....	26
<b>Figure 12.</b> Graphical Representation of the Mean Filter Operation.....	27
<b>Figure 13.</b> The Results of the Pre-processing Methods on Sample Images.....	31
<b>Figure 14.</b> Visualization of the Proposed Tumor Localization Method.....	32
<b>Figure 15.</b> Sample Segmentation Results of the Proposed System.....	38
<b>Figure 16.</b> Comparative Segmentation Results .....	40

## List of Abbreviations

<b>BRATS:</b>	Brain Tumor Segmentation
<b>HGG:</b>	High-Grade Glioma
<b>LGG:</b>	Low-Grade Glioma
<b>MRI:</b>	Magnetic Resonance Imaging
<b>T1:</b>	T1-Weighted
<b>T1C:</b>	T1-Weighted with Contrast Enhancement
<b>T2:</b>	T2-Weighted
<b>FLAIR:</b>	Fluid-Attenuated Inversion Recovery
<b>CNN:</b>	Convolutional Neural Network
<b>TCIA:</b>	The Cancer Imaging Archive
<b>PF:</b>	Potential Field
<b>PR2G:</b>	Patch-Based Updated Run Length Region Growing Technique
<b>IFS:</b>	Infinite Feature Selection
<b>GLCM:</b>	Gray Level Co-Occurrence Matrix
<b>SVM:</b>	Support Vector Machine
<b>WBA:</b>	Whole Brain Atlas
<b>PPV:</b>	Positive Predictive Value
<b>CH:</b>	Calinski-Harabsz
<b>FBB:</b>	Fast Bounding Box
<b>DA:</b>	Dragonfly Algorithm
<b>MRMR:</b>	Minimum Redundancy Maximum Relevance
<b>ERT:</b>	Extremely Randomized Trees
<b>LOOCV:</b>	Leave-One-Out Cross-Validation
<b>RF:</b>	Random Forest
<b>MIPAV:</b>	Medical Image Processing and Visualization
<b>MI:</b>	Mutual Information
<b>MVP:</b>	Multi-View Pointwise
<b>SE:</b>	Squeeze-and-Excitation
<b>LUT:</b>	Lookup Table
<b>JPEG:</b>	Joint Photographic Experts Group
<b>PNG:</b>	Portable Network Graphics

<b>GIF:</b>	Graphics Interchange Format
<b>DCT:</b>	Discrete Cosine Transform
<b>MLP:</b>	Multilayer Perceptron
<b>ReLU:</b>	Rectified Linear Unit
<b>TP:</b>	True Positive
<b>TN:</b>	True Negative
<b>FP:</b>	False Positive
<b>FN:</b>	False Negative

## CHAPTER I

### Introduction

This chapter presents a brief background that includes medical information about brain tumors, the role of the MRI technology in brain tumor diagnosis, the evolution of the brain tumor segmentation systems, and an overview of the proposed system.

#### Background

A brain tumor is the mass of abnormal cells that grows uncontrollably in the brain. The accurate segmentation of the tumors is essential for diagnosis and treatment. Tumors characterized by cancerous and non-cancerous brain cells are classified as malignant and benign. Contrary to the benign tumors' inactive cells content and uniform structure, malignant tumors occur in a non-uniform structure containing active cells. Radiologists frequently predicted gliomas in the glial cells or the spinal cord in recent years. According to the prevalences and high mortality rates, glioma tumors are categorized as HGG and LGG. (Pereira, et al., 2016).

MRI is common for obtaining multimodal images and showing detailed brain structures. Brain MRI images contain four modalities named T1, T1C, T2, and FLAIR, and all of these modalities are available in the sagittal, coronal, and axial planes (Menze, et al., 2015). Healthy brain tissues are analyzed using T1 images when contrast enhancement with the intravenous application of gadolinium is not used. T1C images are used similarly; however, tumor borders are highlighted in these images. The images with the highest intensities are obtained in the T2 images because of the fluids, including tumor edema. FLAIR images attenuate the cerebral fluid and determine the abnormality (Currie, et al., 2013). Even though each modality has a unique representation and process, FLAIR is the most suitable and common one for the segmentation of tumorous regions because of provided abnormality area.

Segmenting brain tumors using MRI images is challenging and time-consuming because of the complex structure of the tumors, which differs in size, shape, location, and appearance (Anitha & Murugavalli, 2016). Therefore, the segmentation of brain tumors is of great importance. Various segmentation methods,



such as thresholding (Amin, et al., 2019; Ilhan & Ilhan, 2017), region growing (Kalaiselvi, et al., 2020), clustering (Eltayeb, et al., 2019), level set (Kermi, et al., 2018; Khalil, et al., 2020) etc., were proposed and implemented for this task. However, these traditional methods are generally proposed as parametric, and the success rates might increase or decrease depending on the values of the selected parameters.

The efficiency of artificial intelligence in producing reasonable human-like decisions and results made machine learning algorithms and deep learning architectures more common on brain tumor segmentation implementations.

The use of machine learning algorithms for the segmentation of brain tumors requires several steps such as further image preprocessing, feature extraction, feature selection, etc. Therefore, the determination of the proper methods and the implementation sequence of these methods have a vital effect on the efficiency of complete brain tumor segmentation (Rehman, et al., 2020; Rehman, et al., 2019; Soltaninejad, et al., 2017).

The efficiency of the CNN in segmentation tasks has gained significant importance with the development of deep learning architectures. CNN has its feature extraction, representation, and learning processes that improve the rates obtained by traditional machine learning algorithms. For that reason, several kinds of studies were performed based on CNN for segmenting complete brain tumors (Ballestar & Vilaplana, 2021; Chithra & Dheepa, 2020; Sohail, et al., 2021; Wu, et al., 2020; Zeineldin, et al., 2020; Zhao, et al., 2021).

The segmentation of the complete brain tumors is considered an essential step in differentiating sub-classes (core and enhancing tumor), and this increases the importance of the achievements and ensures that the studies also continue in this direction.

This study proposes a brain tumor segmentation system based on non-parametric tumor localization and enhancement methods and U-Net architecture. The proposed system segments the brain tumors using the 2D axial images obtained from the patients' FLAIR modalities. The proposed tumor localization and enhancement methods are performed to improve the ability of deep learning architectures in feature extraction, particularly for indistinct tumors. The resultant images obtained from the pre-processing methods are fed to the traditional U-Net architecture, and complete brain tumors are segmented with a high success rate.

Based on the information mentioned above, this study aims:

- to localize and enhance the tumorous regions with proposed non-parametric methods,
- to achieve optimal success rates for the segmentation of the complete brain tumors in three BRATS datasets, and,
- to improve the segmentation abilities of deep learning architectures by providing more distinguishable input tumorous regions.

### **Thesis Layout**

In this thesis, chapter 1 includes a brief background and thesis layout. Chapter 2 is organized as the literature review. Chapter 3 presents the fundamentals of digital image processing. Chapter 4 presents an overview of deep learning and convolutional neural networks basics. Chapter 5 describes the methodology of the study. Chapter 6 presents the results and discussions. Chapter 7 includes the conclusion.

## CHAPTER II

### Literature Review

This chapter analyses recent studies on complete brain tumor segmentation tasks in the literature. These studies are divided into three sections. The first section presents studies that are proposed and implemented in traditional methods. The second section presents studies that include combined systems. The last section presents studies based on CNN architectures.

#### Systems Based on Traditional Methods

Ilhan and Ilhan (2017) proposed a system based on a novel thresholding method for brain tumor segmentation in MRI images. The system was divided into three stages. Initially, the skull was extracted from the image applying morphological and a set of image subtraction operations. The thresholding method was used to segment the tumors in the second stage. The threshold value was calculated as the mean of the unique pixel values in the image, excluding zero. Finally, the noise representing non-tumorous components was removed using a 5x5 median filter. The system was tested on a TCIA dataset named Rembrandt. The overall success rate of the system is 96%.

Amin et al. (2019) proposed a system for brain tumor segmentation in MRI images. The system was divided into three stages. Initially, the Wiener filter was used to remove noise. In the second stage, PF clustering was used to detect the tumorous regions. Finally, the tumorous regions were isolated using global thresholding and morphological operations. The system was tested on T2 and FLAIR images of the BRATS 2013 dataset and evaluated using quality (94%), PPV (96%), sensitivity (97%), specificity (92%), and dice score (0.88) metrics.

Kalaiselvi et al. (2020) proposed a method named PR2G to segment the brain tumors in MRI images. The method was divided into three phases. Initially, the method has classified slices as normal or tumorous using the most significant (determined by the IFS) GLCM features and SVM classifier. In the second phase, the run-length region growing technique was used to segment the tumors from the slices obtained from the previous phase. Lastly, tumor volume construction and estimation were performed using Carelieri's estimator. The method was tested on T2 and

FLAIR slices of the BRATS 2013 dataset and evaluated using dice score (0.80), PPV (82%), sensitivity (98%), and accuracy (84%) metrics.

Eltayeb et al. (2019) proposed a system for brain tumor segmentation in MRI images. The system was divided into three stages. Initially, the slices were classified as non-tumorous or tumorous at the end of several steps. In the first step, the center of the brain region was determined using the center-mass algorithm and its borderline. The slices were divided into two hemispheres using the bounding box and calculated the mean pixel value for both in the second step. In the last step, the tumorous region was localized due to the area under curve calculation. In the second stage, the anisotropic diffusion filter was used to smooth the slices and then the data type of the slices were converted from the grayscale to the CIELAB. In the last stage, k-means clustering was used to segment the tumors, where the k value was determined using the CH cluster validity index. The system was tested on FLAIR slices of the BRATS 2012 (HGG-LGG) dataset and achieved 0.89 and 0.84 dice scores, respectively.

Kermi et al. (2018) proposed a system for brain tumor segmentation in MRI images. The system was divided into two phases. The first phase is pre-processing includes the skull extraction process and filtering operations. The skull was extracted using the FMRIB software library, and the slices were filtered to remove noise using anisotropic diffusion, gradient, and threshold filters. The second phase consists of three steps. In the first step, the slices were divided into two halves as right and left, using the ellipse fitting technique and Otsu's thresholding method. FBB algorithm was applied to detect the tumorous region in the second step. The last step is selecting the slice interest that determines the largest part of the tumorous region. Finally, a combined model forms the region growing and a geodesic level set method was used to segment the tumors. The contour seed point was determined as the centroid of the largest part selected in the previous phase. The system was tested on T2 and FLAIR slices of the BRATS 2017 dataset and evaluated using sensitivity (82% - 89%), fallout (15% - 12%), and kappa (77% - 83%) metrics.

Khalil et al. (2020) proposed a model to segment brain tumors in MRI images. The model was divided into three stages. The first stage is pre-processing includes skull extraction, anisotropic diffusion filter, and contrast enhancement. The skull extraction operation was performed in three steps. Otsu's thresholding method was applied to binarize the slices in the first step. Secondly, morphological

operations were performed to preserve the minute features of the brain region. In the last step, a hole filling operator was applied to obtain a complete-connected brain region. The anisotropic diffusion filter was used to eliminate the noise and increase the homogeneity of the similar regions by preserving their edges. The contrast enhancement was applied using the histogram equalization method to improve the visual appearance of the tumorous region. The second stage is the extraction of the contour seed points using a combined method that includes DA and k-means clustering. In the last stage, contour seed points obtained from the previous stage were initialized to the level set method for segmentation. The model was tested on the BRATS 2017 dataset and evaluated using accuracy (98%), recall (95%), and precision (93%) metrics.

### **Combined Systems**

Soltaninejad et al. (2017) proposed a system that segments the brain tumors in MRI images. The system was divided into four stages. In the first stage, the images were divided into patches with approximately similar size and intensity values using the superpixel method. Statistical, texton and shape features were extracted for each superpixel patch in the second stage. In the third stage, the most significant features were selected using MRMR. Each superpixel patch was classified as tumorous and non-tumorous using SVM and ERT classifiers in the last stage. The system was tested on the FLAIR image of the BRATS 2012 dataset and evaluated using precision, sensitivity, balanced error rate, and dice score metrics. The ERT's performance was reported as superior to the SVM and achieved 89%, 88%, 0.06, and 0.88 precision, sensitivity, balanced error rate, and dice score, respectively.

Rehman et al. (2020) proposed a system to segment the brain tumors in MRI images. The system was divided into three stages. The first stage is pre-processing contains bilateral and Gabor filters. The bilateral filter was used to remove noise, and then the Gabor filter was applied to create the texton map. In the second stage, the images were segmented into superpixel patches. Then, the low-level features were extracted using intensity features and histogram level of texton-map at each patch. A LOOCV was applied at the final stage to classify the image pixels as tumorous and non-tumorous using the classifiers named RF, AdaBoost, RusBoost, and SVM. The system was tested on FLAIR images of the BRATS 2012 (HGG-LGG) dataset and evaluated using accuracy, sensitivity, specificity, precision, and dice score metrics.

The performance of the RF was reported as superior to the others and achieved 98%, 92%, 95%, 88%, and 0.88 accuracy, sensitivity, specificity, precision, and dice score for the HGG images and 96%, 90%, 95%, 86%, and 0.81 for the LGG images.

Rehman et al. (2019) proposed a system to segment brain tumors in MRI images. The system was divided into five stages. The first stage is pre-processing contains skull extraction and noise removal. The skull was extracted using MIPAV. The combination of the bilateral filter and noise threshold using wavelets was applied to remove noise. Secondly, the images were segmented out into superpixel patches and then the intensity, texton map, and fractal features were extracted at each patch. In the third stage, the features were normalized and then the most significant ones were selected using the MI-based feature selection method. In the fourth stage, in order not to adversely affect the performance of the classifiers, the imbalance in the feature matrix that forms due to a close or the unequal number of observations in each class was prevented by a class balancing operation. In the last stage, the image pixels were classified as tumorous and non-tumorous using SVM, AdaBoost, and RF classifiers. The system was tested on FLAIR images of the BRATS 2012 dataset and evaluated using precision, sensitivity, specificity, balance error rate, and dice score metrics. The performance of the RF was reported as superior to the others and achieved 89%, 93%, 97%, 0.1, and 0.91 precision, sensitivity, specificity, balance error rate, and dice score, respectively.

### **CNN Based Systems**

Wu et al. (2020) proposed an architecture named DCNN-F-SVM to segment the brain tumors in MRI images. The model was divided into three phases. In the first phase, a DCNN was trained to map from the image domain to the tumor marker domain. The predicted labels from the DCNN training were fed to the integrated SVM classifier at the second phase and test images. Finally, a DCNN and an integrated SVM were connected in series to train a deep classifier. The DCNN-F-SVM architecture was tested on the BRATS 2018 and the self-made datasets and evaluated using dice score, sensitivity, and specificity metrics. The performance of the architecture was reported as superior to the DCNN and integrated SVM and achieved 0.90, 91%, and 99.8% dice score, sensitivity, and specificity for the BRATS 2018 dataset and 0.90, 92%, and 98.8% for the self-made dataset.

Chithra et al. (2020) proposed a system that includes a CNN architecture based on Di-phase midway for brain tumor segmentation in MRI images. The system was divided into two phases. The first phase is pre-processing contains N4ITK bias field correction and noise removal. The N4ITK bias field correction method was applied to correct the intensity variations of the images, and then the noise was removed using the median filter. The enhanced images were fed to the Di-phase midway based CNN architecture to segment the tumors in the second phase. The system was tested on the BRATS 2012, BRATS 2013, and BRATS 2018 datasets (HGG-LGG) and evaluated using accuracy, sensitivity, and dice score metrics. The accuracy, sensitivity, and dice score obtained from the BRATS 2012 dataset were 94%, 89%, and 0.84 for the HGG images and 95%, 86%, and 0.85 for the LGG images. The system achieved 97%, 88%, and 0.91 accuracy, sensitivity, and dice score for the HGG images of the BRATS 2013 dataset and 92%, 87%, and 0.87 for the LGG images. Finally, the accuracy, sensitivity, and dice score for the BRATS 2018 dataset were reported as 95%, 89%, and 0.90 for the HGG images and 93%, 94%, and 0.89 for the LGG images.

Zeineldin et al. (2020) proposed an architecture named DeepSeg to segment the brain tumors in MRI images. The architecture design can be analyzed in two phases. The U-Net architecture was modified in the first phase by rearranging the layers. In the second phase, the encoder part of the modified U-Net was replaced using the CNN architectures named VGGNet, ResNet, DenseNet, Xception, MobileNet, NASNet, and MobileNetV2. The architecture was trained using the k-fold cross-validation, where the k value was determined as two. Before the training process, the count of the training samples was increased using various data augmentation techniques such as flip, rotate, elastic transformation, etc., to prevent the overfitting problem. The architecture was tested on the BRATS 2019 dataset and evaluated using sensitivity, specificity, Hausdorff distance, and dice score metrics. The performance of the Xception/modified U-Net combination was reported as superior to the others and achieved 0.86%, 99.8%, 11.337, and 0.84 sensitivity, specificity, Hausdorff distance, and dice score, respectively.

Sohail et al. (2021) proposed a system based on a 3D U-Net for brain tumor segmentation in MRI images. The system was divided into two stages. The first stage is pre-processing includes crop, data normalization and splitting, random patch extraction, and data augmentation operations. The brain regions of the input images

were cropped to reduce the input data size and just keep only the useful information. The cropped images were enhanced by using a normalization method to make them more suitable for the segmentation. The split operation was applied to determine the number of data in training (82%), validation (6%), and testing (12%) sets. To avoid any hardware problem while training with large volumetric data, random patches were extracted from the input data. The augmentation techniques, such as rotating and mirroring, were applied to prevent the overfitting problem. Finally, a 3D U-Net architecture was used to segment the tumors. The system was tested on the BRATS 2019 and BRATS 2020 datasets and achieved 0.78 and 0.72 dice scores, respectively.

Zhao et al. (2021) proposed an architecture named MVP U-Net to segment the brain tumors in MRI images. The architecture has the same design as the 3D U-Net architecture, except for the structural difference of the convolutional layers. The convolutional layers of the architecture were replaced with three 2D multi-view convolutions to learn spatial features and one pointwise convolution to learn channel features. Further, The SE block was modified to integrate it into the architecture after the concatenation operation. In this way, it was thought that the capabilities of the architecture could be increased, and the count of parameters could be reduced. Before the training process, various pre-processing techniques were applied to the images. Initially, the brain regions of the images were cropped and normalized to reduce the input size and just keep only the useful information. Further, the count of the training samples was increased using various augmentation techniques such as rotation, scaling, etc., to prevent the overfitting problem. The architecture was tested on the BRATS 2020 dataset and achieved 91%, 0.80, 99.7%, and 29.831 sensitivity, dice score, specificity, and Hausdorff95, respectively.

Ballestar and Vilaplana (2021) proposed a system based on V-Net and the variations of 3D U-Net for brain tumor segmentation in MRI images. The system was divided into three stages. The first stage is pre-processing, which includes data normalization, and augmentation was applied to make the images more suitable for the segmentation and prevent the overfitting problem. To avoid any hardware problems in the training process due to the large volumetric data, a patch extraction operation was performed at the second stage using either binary or random tumor distribution approaches. In the last stage, the V-Net and variations of 3D U-Net architecture were used to segment the tumors. The system was tested on the BRATS



2020 dataset and evaluated using dice score and Hausdorff95 metrics. The performance of the V-Net architecture was reported as superior to the variations of 3D U-Net architecture and achieved 0.87 and 10.19 dice score and Hausdorff95, respectively.

## CHAPTER III

### Digital Image Processing

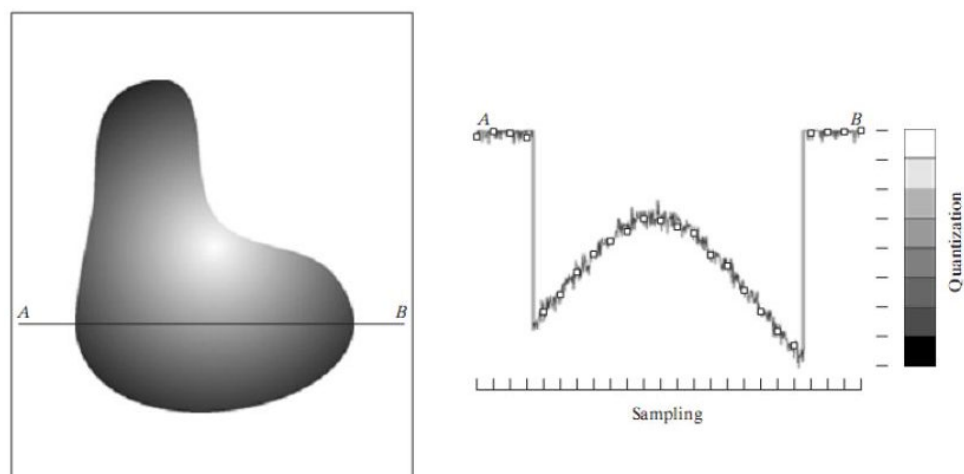
This chapter presents an overview of digital image processing fundamentals including image acquisition, compression, enhancement, and segmentation.

#### Image Acquisition

The first stage of digital image processing is acquisition. Digital image processing is transferring the image from the sensors to the computer and transmitting it to the output after any operation is done on it. The hardware and software used for image acquisition may differ depending on the image source. Converting real-world 3-D objects into digital images; obtained from sources such as CCD and infrared cameras, ultrasound equipment, X-ray, MRI instruments, and satellites. The output of the sensor is a continuous voltage wave whose amplitude and spatial behavior change depending on the phenomenon being viewed. It is necessary to digitize this continuous data for digital image acquisition. Two processes are required for this, called sampling and quantization. The resulting image function  $f(x,y)$  can be continuous in its coordinates and amplitude. For a digital image, it is necessary to do both separately. If coordinate values are digitized, it is called sampling; if amplitude values are digitized, it is called quantization (Gonzalez & Woods, 2002). Figure 1 shows the sampling and quantization of digital images.

Figure 1.

*The Sampling and Quantization of Digital Images.*

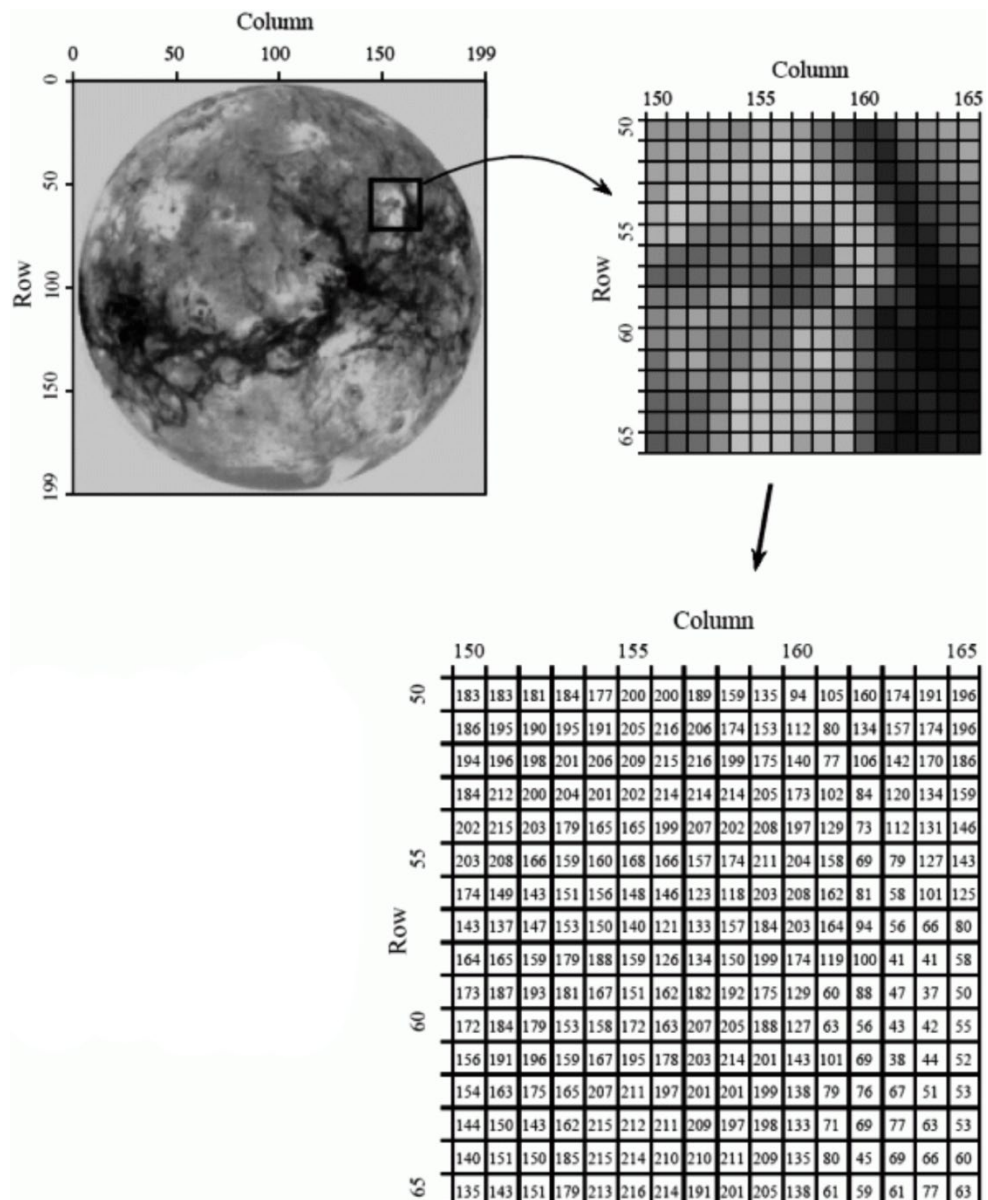


### *Digital Image*

A digital image can be considered a matrix of elements whose row and column indices define any point in the image. Each element of this matrix contains information about the color of that point and is called a pixel (Gonzalez & Woods, 2002). Figure 2 shows the basic structure of digital images.

Figure 2.

*Basic Structure of Digital Images.*

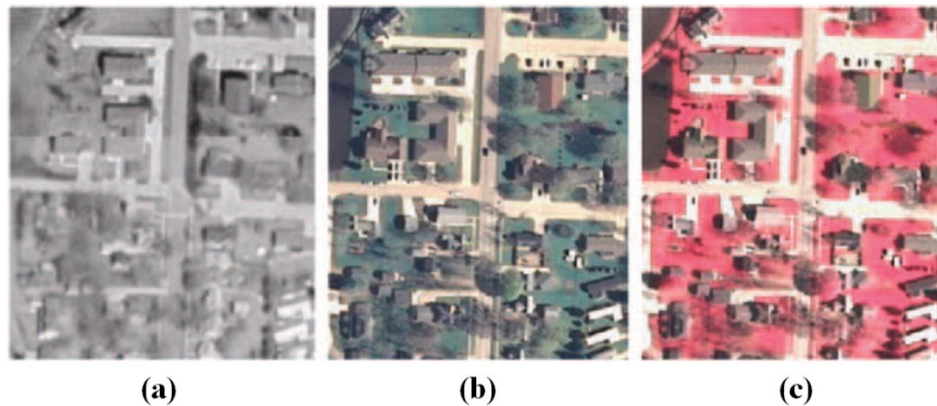


Digital images are divided into three groups named gray-level, color, and multi-spectrum. Figure 3 demonstrates sample images that represent each digital image group.

- **Gray-Level Images:** These are monochrome images containing only intensity information.
- **Color Images:** These are composed of overlapping three gray-level images coded as R(Red), G(Green), B(Blue).
- **Multi-Spectrum Images:** These are images obtained from regions outside the visible spectrum, also called false-color images.

Figure 3.

*Sample Images for Each Digital Image Group.*



Where (a) gray-level image, (b) color image, and (c) multi-spectrum image

Resolution is defined as the product of the number of rows and columns in an image (Gonzalez & Woods, 2002). The resolution does not include information about the size of the image since the size is not valid for pixels; however, as the resolution decreases (as the number of pixels in the image decreases), the pixelation increases, as shown in Figure 4.

Figure 4.

*Pixelation on Digital Images.*

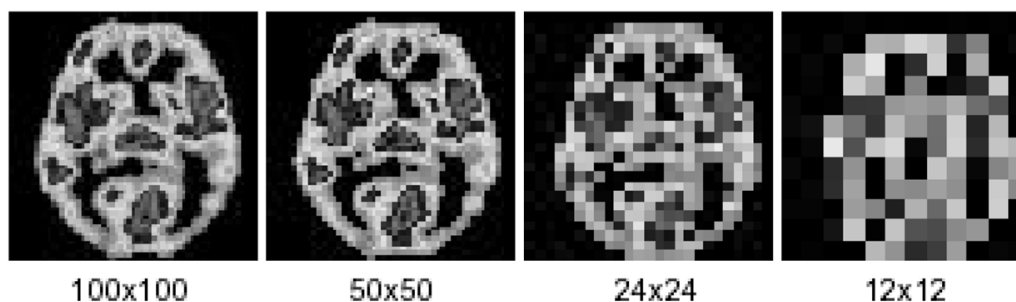


## **Image Compression**

The major challenge of digital image processing is its large size and the lengthy time it takes to process them. In most cases, digital image processing software can't be improved in terms of the speed of processing such large image files. Instead, the image sizes can be reduced to increase the processing speed of the software at runtime. By employing file compression methods, it is possible to reduce the image size to more manageable file size and speed up the processing power of the application software in execution (Hussain, et al., 2018).

The file compression removes the redundant data bits representing pixels on the image so that the image size is minimized without losing its characteristics. As a result, the image size becomes more manageable, resulting in increased processing speed and reduced storage area in the system (Hussain, et al., 2018). There are three different ways of removing redundant data.

### ***Inter-Pixel Redundancy***

In this method, the algorithm assumes that each pixel's neighbors have similar characteristics and are not very different; therefore, they are regarded as redundant pixels and can be represented with the same pixel value. This type of redundancy is named as Inter-Pixel redundancy. Among others, one popular way of detecting redundant pixels is to evaluate the characteristics of their neighboring pixels (Kapoor & Kaushik, 2018).

### ***Coding Redundancy***

The method builds a variable-length data code representing a pattern of pixels and runs a search routine to find the exact match in the original image file. A LUT is used, keeping such search codes and fed into the system, in turn, to locate their exact matches and remove them from the image file. The same (LUT) can also reverse the removal process of redundant code strings to avoid data loss. Two popular methods of detecting redundant formations of pixels are The Huffman codes and the arithmetic coding (Kapoor & Kaushik, 2018).

### ***Psychovisual Redundancy***

Because of the complexity in human vision characteristics from the point of view of psychophysics, not every visual signal sensed equally well comes because of

the eye. The human brain assesses and categorizes the signals as important and not so important classes. The not so important signals are considered redundant and removed from the image. The DCT is a popular representation of this type of approach and is the basis of the JPEG encoding standard (Kapoor & Kaushik, 2018).

### ***Compression Methods***

Depending on the requirements the image compression can be classified into two types named lossy and lossless (Hussain, et al., 2018).

**Lossy Compression Technique.** This type of compression works on JPEG images. During compression, this technique causes some data loss. As a result, the compressed image does not have the same characteristics as the original one but looks very similar. The algorithm will produce a compressed image that resembles and loosely represent the original one. Although there is a broad application of this technique, it is not suitable in digital image processing for medical use (Kapoor & Kaushik, 2018).

**Lossless Compression Technique.** In this compression type, an exact copy of the original image is produced with reduced file size by encoding technique. File types such as GIF and PNG are the popular representation of lossless compression techniques (Kapoor & Kaushik, 2018).

### **Image Enhancement**

Image enhancement is used to improve the image quality where there are blurred areas that make it difficult to process properly. The characteristics of the image become more visible thru the improved contrast and hence more suitable for processing activities.

There are two different methods used named spatial and frequency domain. These methods are not very objective due to the various operators' different interpretations of the images (Gonzalez & Woods, 2002).

### ***Spatial Domain***

With Equation 1, the image is directly transformed by manipulating the pixels and those around it (Gonzalez & Woods, 2002).

$$g(x, y) = T[f(x, y)] \quad (1)$$

The input image is represented by  $f(x, y)$ , the transformation operator  $T$  works on the input image neighborhood. As a result, an output image  $g(x, y)$  is produced. In most cases, the spatial domain type of work uses this method.

### ***Frequency Domain***

This method is used to minimize the noise. The noise reduction helps to identify the domain. The Fourier transformation is used as the first step. Then, the image's brightness and contrast are improved by using an image enhancement operation. This operation also distributes the grey levels (Gonzalez & Woods, 2002). Equation 2 is established as a result.

$$G(u, v) = H(u, v) F(u, v) \quad (2)$$

In this method,  $F$  represents the initial image,  $H$  represents the transformation function, and  $G$  represents the resultant image.  $F(u, v)$  represents the Fourier transformed image. As a result, different frequency values of  $F(u, v)$  are obtained. The low frequencies represent the smooth or blurred areas in the image, and the details of the image are represented by the high frequencies, edges, and noise. (Gonzalez & Woods, 2008).

### **Image Segmentation**

Image segmentation is carried out to distinguish the object of interest from the rest of the image. The extraction of the part representing the object then becomes more visible and perhaps becomes a better-defined area to be offered for investigation. This process is very successful and hence is quite popular for locating the objects in an image by identifying its boundaries (Gonzalez & Woods, 2008).

Supposing that  $R$  is the whole of the area covered by some image. The segmentation process can then be regarded as a process that partitions this area into  $n$  sub-regions as  $R_1, R_2, R_3$ , and so on, as in Figure 5.

Figure 5.

*The Process for How a Segmentation Technique Works.*

- a.  $\bigcup_{i=1}^n R_i = R$
- b.  $R_i$  is a connected set,  $i=1,2,\dots,n$ .
- c.  $R_i \cup R_j = \emptyset$  for all  $i$  and  $j$ ,  $i \neq j$ .
- d.  $Q(R_i) = \text{TRUE}$  for  $i= 1,2,\dots,n$ .
- e.  $Q(R_i \cup R_j) = \text{FALSE}$  for any adjacent regions  $R_i$  and  $R_j$ .

The steps in Figure 5 shows that  $Q(R_k)$  is a logical predicate on the points registered in the set  $R_k$ . Here the null set is represented by  $\emptyset$ . the sets union and intersection operations are represented by the  $\cup$  and  $\cap$  symbols respectively (Gonzalez & Woods, 2008). The resultant regions  $R_i$  and  $R_j$  become adjacent when their union makes a connected set. This is possible under some conditions indicated by (a) where every pixel is in the region so that the segmentation is complete and (b) where points in the region are connected in a predefined way. The following example shows how the method works.

The points in the set should be 4- or 8- connected. Step (c) says that the regions should be disjoint, and step (d) points out that the properties which are to be satisfied by the pixels should be in the segmented area. In that case,  $Q(R_i)$  is *TRUE* only if all the pixels in  $R_i$  belong to the same level of identity. In the end, step (e) indicates that two adjacent regions,  $R_i$  and  $R_j$ , must differ so that they satisfy the predicate  $Q$ . A fundamental problem exists in the segmentation process to partition the images into regions that satisfy the initial conditions (Gonzalez & Woods, 2008).



## CHAPTER IV

### Deep Learning and Convolutional Neural Networks

This chapter presents the description of deep learning, the CNN basics and their architectures proposed for image segmentation tasks.

#### Deep Learning

Deep learning methods are used in many everyday applications ranging from speech and handwritten character recognition to diverse image and object identification tasks. They are representation-learning approaches, taking raw data as input and subject to a learning process to uncover valuable features instead of depending on hand-tuned feature extractors. Deep learning architectures consist of numerous layers composed of basic modules susceptible to learning and learn representations. Each layer provides a somewhat more abstract and “useful” representation (LeCun, et al., 2015).

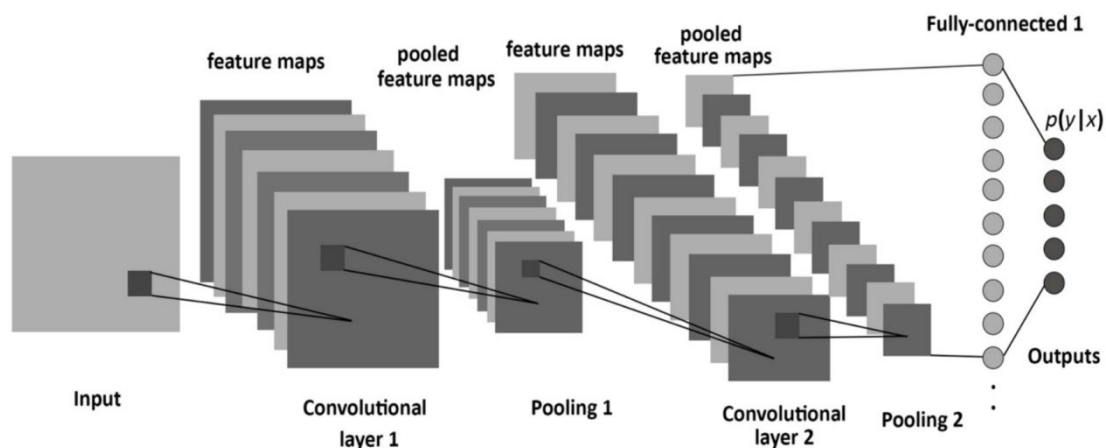
#### Convolutional Neural Networks

CNNs are a kind of feedforward neural network built for image processing. It was initially described in 1989 by LeCun, who designed it for hand-written digit identification. CNN was also one of the first neural networks to be employed in commercial applications. AT&T used a convolutional network in a real-world bank system that recognizes hand-written numbers in cheques as early as 1990. CNNs are now engaged in most computer vision tasks to solve various object identification difficulties and more demanding tasks (LeCun, et al., 2015).

CNN has the benefit of being able to be applied to structured data. The network’s input is a multidimensional array. A grayscale input image is represented by a 2D array, with each integer describing one pixel. A 3D array represents a color image where a vector of color values describes each pixel. A CNN may be trained on 1D sequences such as printed text or sound signals. A convolutional network’s neurons are organized in a grid and consider the connection between neighboring data samples (LeCun, et al., 2015). Figure 6 shows a sample of CNN architectures.

Figure 6.

*Sample CNN Architecture.*



### ***Convolution Operation***

CNNs get their name from the linear mathematical operation convolution. Convolution in image processing is a two-matrix operation ( $I \times K$ ), where  $I$  is an input vector and  $K$  is a kernel (convolutional matrix). This operation gives each matrix position's weighted sum of the input matrix values in a local neighborhood. The kernel specifies the neighborhood's weights and size (Yamashita, et al., 2018).

The same operation is used to compute a neuron's inner potential in the context of CNNs. The kernel is an odd-sized weight matrix. The most common kernel sizes range from  $3 \times 3$  to  $9 \times 9$  pixels. Compared to the convolutional matrix utilized in image processing, the CNN kernel is entirely learnable. It is capable of adapting to patterns in training data. The convolution is employed as a pattern detector. Distinct kernels define distinct patterns and are recognized on various levels. Each network layer indicates a different detection level. Early layers recognize simple patterns, such as edges in various orientations, colors, or gradients. Later layers recognize more complicated patterns as a composite of simple ones (Yamashita, et al., 2018).

### ***Convolutional Layer***

The convolutional layer is the essential component of a CNN's design. It is a layer of neurons that uses convolution to calculate their inner potential. A convolutional layer's neurons have a fixed location in a grid. The grid of these neurons is referred to as a feature map. A kernel supplies weights of their

connectivity. There might be numerous feature maps inside one convolutional layer that perform simultaneously on the same data. Each feature map employs its kernel (Yamashita, et al., 2018).

Several settings may be applied to the convolutional layer to alter the layer's behavior and the size of the feature maps. The most common settings are stride and padding. The stride is a number that describes the distance between the two nearest kernel positions. Convolution will be calculated for each position if stride equals one. If stride equals two, the result is calculated only in every second position. As a result, a feature map is downsampled by two. The padding sets calculation in border positions. Convolution cannot be calculated for pixels with a neighborhood outside of the image domain. The addition of zero padding around the input image might be a solution (Yamashita, et al., 2018).

It's known as the same padding in CNN terminology. To avoid contaminating the computation with zeros, we can only calculate convolution at valid locations. The size of the feature map is then reduced by  $2k-1$  pixels, where the  $k$  is a kernel dimension. This is known as valid padding. There are two main reasons why CNNs outperform MLP on image data. (Pang, et al., 2017).

**Sparse Connectivity.** The sparse connection is pertained to the kernel dimension being less than the image size. An input may contain millions of pixels, but a conventional kernel only has maximum hundred values. Using just a few weights, we can create a feature map with the same dimension as the input. If we want to produce an output the same size as the MLP input, the number of weights must equal the square of the input size. The convolutional layer significantly decreases memory requirements as well as learning runtime. It enables high-resolution image processing without the need for downsampling (Pang, et al., 2017).

**Parameter Sharing.** The term parameter sharing refers to a single kernel being utilized several times at distinct image positions. For example, if the kernel is trained to recognize a vertical edge, it will recognize it in every other location in the image. This also implies that each kernel is trained on more data than the number of training samples in all of these locations. It enhances the likelihood that the kernel will be well learned (Pang, et al., 2017).

### ***Pooling Layer***

A pooling layer is a neural network layer that does not have learnable parameters. It downsamples the input by performing the specified statistics of the nearby units, e.g., maximum, mean. The pooling layer ensures that network performance is unaffected by tiny translations. For example, small disparities in facial motions may be eliminated in face detection. They are the basic components of CNNs, together with the convolutional layer (Yamashita, et al., 2018).

### ***Fully Connected Layer***

The output feature maps of the last convolutional layer are flattened, and a 1D array of numbers are created. These layers are then get connected to at least one fully connected layer. Each input and output are connected using a learnable weight. When the required features by the convolutional layers are extracted and the pooling layers downsampled and generate them, they are sent to the network's final outputs by a subset of fully connected layers. It is typical to find that the fully connected layers and the classes will have the same output nodes in the end. Each following fully connected layer, there is a ReLU nonlinear function (Yamashita, et al., 2018).

## **CNN Architectures for Image Segmentation**

In recent years, various CNN architectures have been proposed to perform image segmentation tasks. The most common of these architectures are SegNet and U-Net.

### ***SegNet***

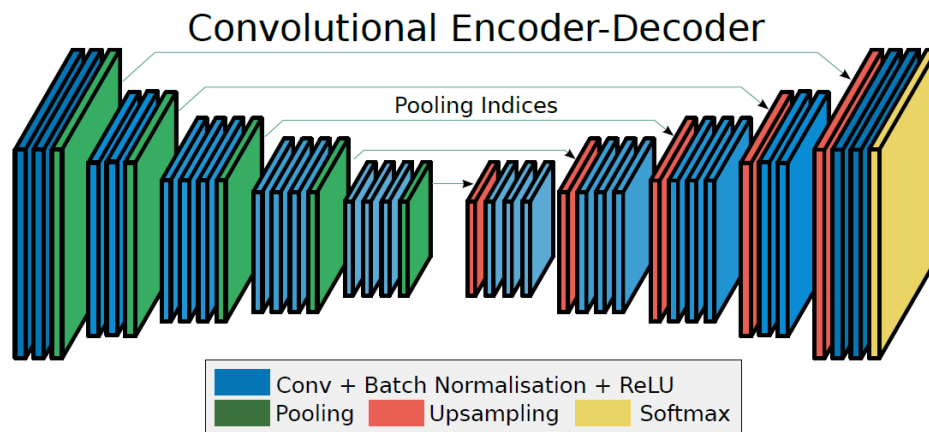
The SegNet architecture (Badrinarayanan, et al., 2017) comprises an encoder path, a decoder path that corresponds to it, and a pixel classification layer. In the VGG16 network, 13 convolutional layers occur in the encoder root, corresponding to the first 13 convolutional layers. Having every encoder layer correspond to each decoder layer means that the decoder network has 13 convolutional layers. In the end, the resultant decoder layer goes through a multi-class softmax classifier, generating class probabilities of each pixel.

The encoder path contains five convolution blocks. A max-pooling operation follows every block with a 2x2 window and a stride 2 for downsampling. Every convolution block is made of a number of layers which are 3x3 convolution with

batch normalization and element-wise ReLU. Here initial two convolution blocks have two layers each, and three blocks have three layers each. The decoder path and the encoder path are symmetric; The only difference is that an upsampling process is used instead of the max-pooling process. The outputs of the preceding layer and the indices of the max-pooling of the corresponding encoding layer become inputs for the upsampling. The resultant decoder path, a high-dimensional feature representation, is fed into a soft-max classifier and classifies every pixel. The SegNet architecture is shown in Figure 7.

Figure 7.

*SegNet Architecture.*



### *U-Net*

The U-Net architecture (Ronneberger, et al., 2015) was developed to provide a more efficient segmentation of biomedical images and has been widely used in studies that focused on this task.

Wang et al. (2018) and Karthik et al. (2019) used traditional U-Net architecture to segment the rectal tumors and the ischemic lesion, respectively. Tong et al. (2018) modified the U-Net architecture to segment the pulmonary nodules. Rundo et al. (2019) proposed an architecture named USE-Net for zonal prostate segmentation. Song et al. (2020) proposed an architecture named BSU-Net to segment the liver tumors. Li et al. (2020) proposed an architecture named MRBSU-Net for gastrointestinal stromal tumor segmentation. The U-Net architecture consists of two paths named contraction and expansion.

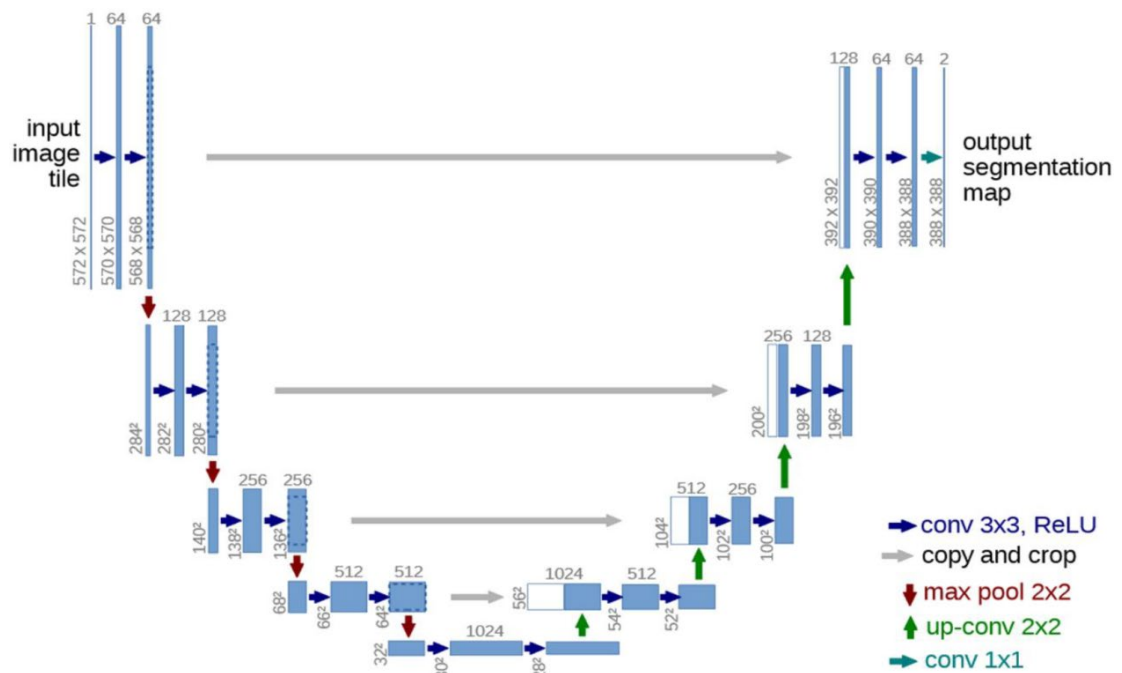
The contraction path, also known as the encoder, consists of a series of blocks and each block includes two 3x3 convolutional layers, each followed by a ReLU, and a 2x2 maximum pooling operation with stride 2. After each block, the number of feature maps is doubled, thus enabling the architecture to learn complex structures more effectively.

The expansion path, also known as the decoder, has a similar design to the contraction path. Each block contains a 2x2 up-convolutional layer, and two 3x3 convolutional layers, each followed by a ReLU. At the end of each block, the number of feature maps is halved to maintain symmetry. However, the feature map of each up-convolutional layer is concatenated with the cropped feature map of the corresponding contraction layer. This allows the features learned when contracting the image to be used to reconstruct itself. Cropping is required because of the loss of border pixels at each convolution operation.

Finally, pass through a 1x1 convolutional layer with a number of feature maps equal to the desired number of classes, and then pixel-wise softmax activation and cross-entropy loss functions are applied to the resultant feature map. In this way, each pixel in the image is classified as belonging to a class. Figure 8 demonstrates the U-Net architecture.

Figure 8.

*U-Net Architecture.*



## CHAPTER V

### Methodology

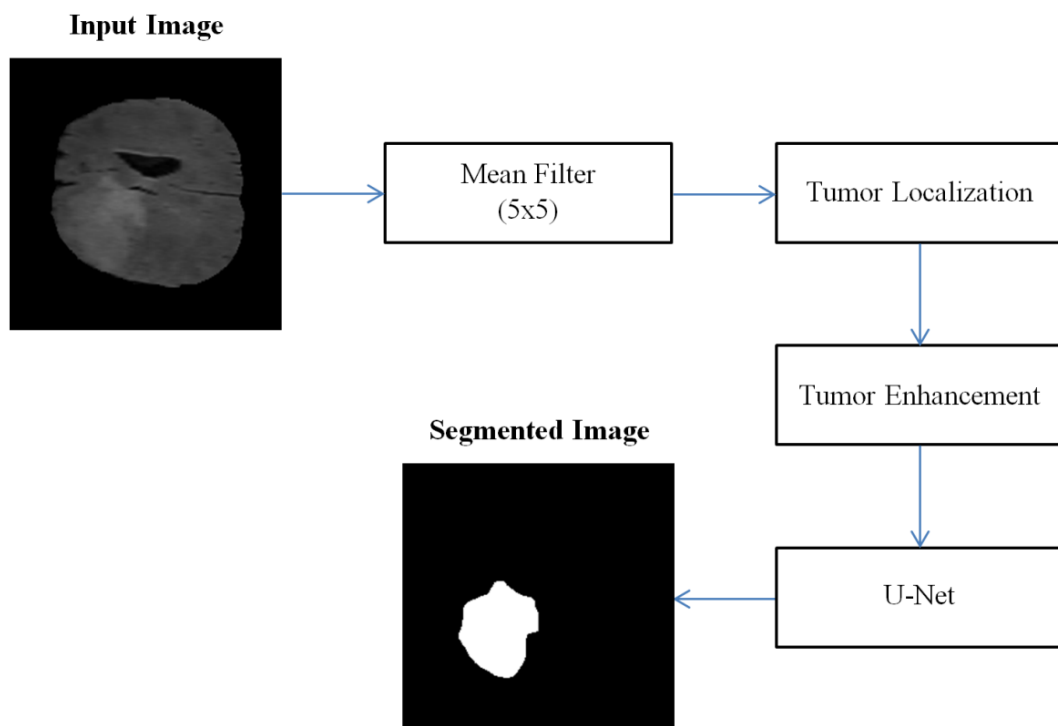
This chapter presents the methodology of the study. The methodology is divided into two sections. The first section describes the proposed system in detail. In the second section, the evaluation metrics used to measure the performance of the proposed system are presented.

#### Proposed System

The proposed system is divided into three stages. Initially, all tumorous images are filtered using a 5x5 mean filter to remove noise. In the second stage, the proposed tumor localization and enhancement methods are applied to make the images more suitable for the segmentation process by increasing the visual appearance of the tumorous regions. Lastly, the traditional U-Net architecture is used to perform the segmentation of the tumors on resultant images obtained from the pre-processing methods. Figure 9 shows the block diagram of the proposed system.

Figure 9.

*The Block Diagram of the Proposed System.*



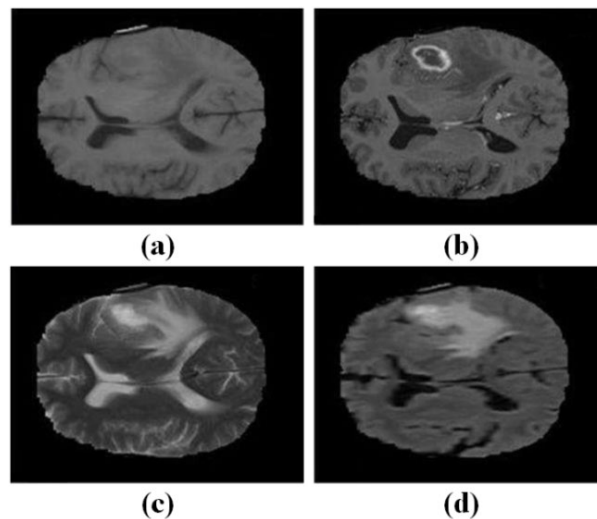
### ***Dataset***

This study considered three common and recent BRATS datasets named BRATS 2012, BRATS 2019, and BRATS 2020 to evaluate the proposed system (Bakas, et al., 2017; Bakas, et al., 2018; Menze, et al., 2015).

Each image in the BRATS datasets consists of four modalities as T1, T1C, T2, and FLAIR. The images are skull stripped and the experienced radiologists annotated their ground truths. Figure 10 demonstrates the sample images of modalities.

Figure 10.

*Sample Images for Modalities.*



Where (a) T1, (b) T1C, (c) T2, and (d) FLAIR.

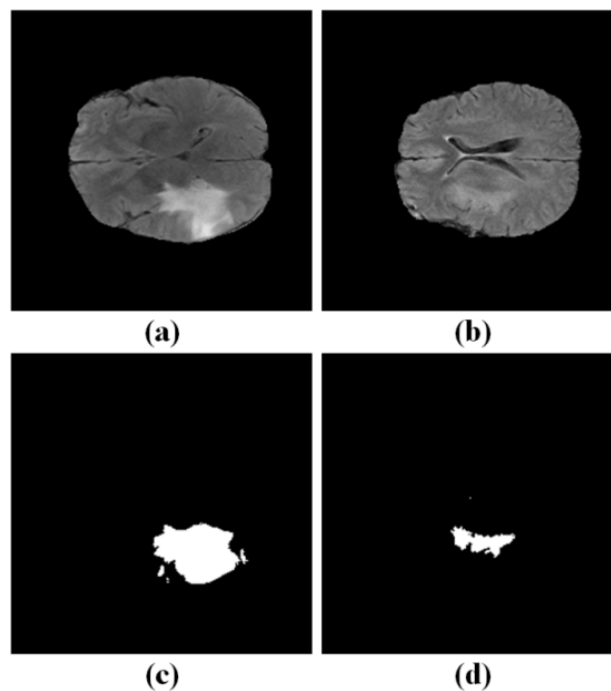
BRATS 2012 is the most commonly used dataset for the complete brain tumor segmentation task and consists of 30 patients. The number of 2D axial FLAIR images (tumorous and non-tumorous) of the patients is 5,633. One of the recent versions of the BRATS datasets is 2019 and includes 335 patients. The number of 2D axial FLAIR images (tumorous and non-tumorous) of the patients is 51,925. The final version of the BRATS dataset was released in 2020 and contains 369 patients. The number of 2D axial FLAIR images (tumorous and non-tumorous) of the patients is 57,195. A more detailed description of the considered datasets is presented in Appendix D.



Figure 11 demonstrates the challenge of the brain tumor segmentation for distinct and indistinct tumorous images and their corresponding complete tumor ground truths.

Figure 11.

*Samples for Distinct and Indistinct Tumorous Images.*



Where (a) distinct tumorous region, (b) indistinct tumorous region, (c) complete tumor ground truth of the image (a), and (d) complete tumor ground truth of the image (b).

### ***Mean Filter***

One of the most common problems faced in digital image processing is noise. Image filtering methods are used as a pre-processing method to overcome this problem. The mean (average) filter is one of the most widely used image filtering methods. The mean filter works by manipulating each pixel value in the image with an average value that includes its neighbors and itself. This process removes pixel values from the images that do not represent the surroundings. The mean filter is one of the convolution filters and like the others, it is based on a kernel representing the neighborhood shape and size to be determined when computing the mean (Gonzalez & Woods, 2008). The mean filter operation is depicted in Figure 12.

Figure 12.

*Graphical Representation of the Mean Filter Operation.*

Original		
5	3	6
2	1	9
8	4	7

$$5 + 3 + 6 + 2 + 1 + 9 + 8 + 4 + 7 = 45$$

$$45 / 9 = 5$$

Mean Filtered		
*	*	*
*	5	*
*	*	*

### ***Proposed Tumor Localization and Enhancement Methods***

In the first step of the proposed tumor localization method, the background and tumorous regions are determined using the image histogram. A histogram provides the frequency distribution of the intensity values in the image (Burger & Burge, 2016). While the background and the frames of images that do not consist of any information regarding the brain MRI images are represented as black, the zero intensity values are excluded from the obtained image histogram. The frequency of each intensity value excluding zero is calculated using an image histogram and shown in Equation 3:

$$n_j = \sum_{j=1}^{k-1} I_j \quad (3)$$

Where  $j$  is the range between 1 and  $k-1$ ,  $n_j$  is the histogram value of  $j^{th}$  intensity value of the image, and  $I_j$  is defined as in Equation 4:

$$I_{(x,y)} \in [0, k - 1] \quad (4)$$

Where  $x$  and  $y$  are the spatial coordinates of the image and  $k$  is the maximum intensity range within the image.

The second step of the proposed method is to determine the initial non-parametric threshold value  $\Theta_{fr}$  using frequencies of the intensity values obtained by the image histogram in order to optimize the determination of background, irrelevant, and the most informative regions within the image while the most frequent intensity values in brain MRI images represent the healthy brain tissues and tumorous region. The  $\Theta_{fr}$ , which can be described as the mean of intensity frequencies, is calculated as shown in Equation 5.

$$\theta_{fr} = \frac{1}{k-1} \sum_{j=1}^{k-1} n_j \quad (5)$$

Since all tumors do not appear significantly in the MRI images, the following steps of the proposed method aim to determine the tumorous region in the image as a significant or low-contrast tumor to provide robust enhancement before the segmentation process.

The  $\Theta_{fr}$  is used to determine the  $B_{min}$  and  $T_{min}$  values that represent the minimum values for the background and tumorous regions using the Equations 6 and 7:

$$B_{min} = \min(I_{\theta_{fr}}) \quad (6)$$

$$T_{min} = \max(I_{\theta_{fr}}) \quad (7)$$

Where  $I_{\theta_{fr}}$  is the intensity values where the frequencies are more than  $\Theta_{fr}$ . The calculation of  $B_{min}$  and  $T_{min}$  provided us to initially localize the tumorous region, where  $B_{min} < T_{min}$  is the background and  $T_{min} < k-1$  is the tumorous region.

Our hypothesis is that if the tumorous region's standard deviation is higher than the standard deviation of the background region, the tumor could easily be distinguished and segmented. Otherwise, the localization of background and tumorous regions requires further processing since the low-contrast appearance of brain tumors that are not significantly distinguishable from the healthy brain tissues.

Therefore, we used a fundamental statistical approach, standard deviation (Allen, 2017), to determine the distinguishability and contrast between the background and tumorous regions. The standard deviations of the background and tumorous regions are calculated using Equations 8 and 9:

$$Std_B = \sqrt{\frac{\sum(I_{iB} - m_B)^2}{n_B}} \quad (8)$$

$$Std_T = \sqrt{\frac{\sum(I_{iT} - m_T)^2}{n_T}} \quad (9)$$

Where  $I_i$ ,  $m$ , and  $n$  represent intensity value, mean value, and the number of pixels belonging to the background ( $B$ ) and tumorous ( $T$ ) regions.

After localization and the determination of the contrast level of the tumor, we propose a tumor enhancement method that significantly increases the visual appearance of the tumorous region even it is low-contrast or not.

Our enhancement method and final localization are based on the conditions after comparing the standard deviations obtained for both background and tumorous regions. Similar to our hypothesis mentioned above, the tumor is localized in the initial background region if the background region's standard deviation is higher than the initial tumorous region. Otherwise, it is localized in the initial tumorous region. The formula of final localization is given in Equation 10:

$$\begin{cases} B & \text{if } Std_B > Std_T \\ T & \text{if } Std_B < Std_T \end{cases} \quad (10)$$

Where  $B$  and  $T$  denote the background and tumorous regions, respectively.

After the final localization, the proposed enhancement method is applied to the localized tumorous region and ignored the empty region to make the tumorous region more significant. Our enhancement method uses two stages for low-contrast and distinguishable tumors according to the localized regions. First, it considers the minimum value and the standard deviation of the tumorous region to make the intensity values of the tumor more significant if the tumor is localized in the  $T$  region, as shown in Equation 11.

$$O_T = \frac{I_{T(x,y)} - T_{min}}{Std_T} \quad (11)$$

However, our proposed enhancement method considers the updated minimum value for the tumorous region and the updated standard deviation to make the low-contrast tumor more significant if the tumor is localized in the  $B$  region. The formula of updated tumorous region  $T_{U_{min}}$  and  $Std_{T_U}$  are shown in Equation 12 and 13.

$$T_{U_{min}} = \frac{1}{x} \sum_{j=B_{min}}^{k-1} I_j \quad (12)$$

Where  $T_{U_{min}}$  is the updated minimum value of the tumorous region and is defined as the mean intensity values between  $B_{min}$  and  $k-1$ , and  $x$  represents the pixel within the region.

$$Std_{T_U} = \sqrt{\frac{\sum (I_{iT_U} - m_{T_U})^2}{n_{T_U}}} \quad (13)$$

Where  $I_{iT_U}$ ,  $m_{T_U}$ , and  $n_{T_U}$  represent intensity value, mean value, and the number of pixels belonging to the updated tumorous region ( $T_{U_{min}}$ ).

Therefore, the final enhancement for the low-contrast and indistinct tumorous region is calculated as given below in Equation 14.

$$O_B = \frac{I_{T(x,y)} - T_{U_{min}}}{Std_{T_U}} \quad (14)$$

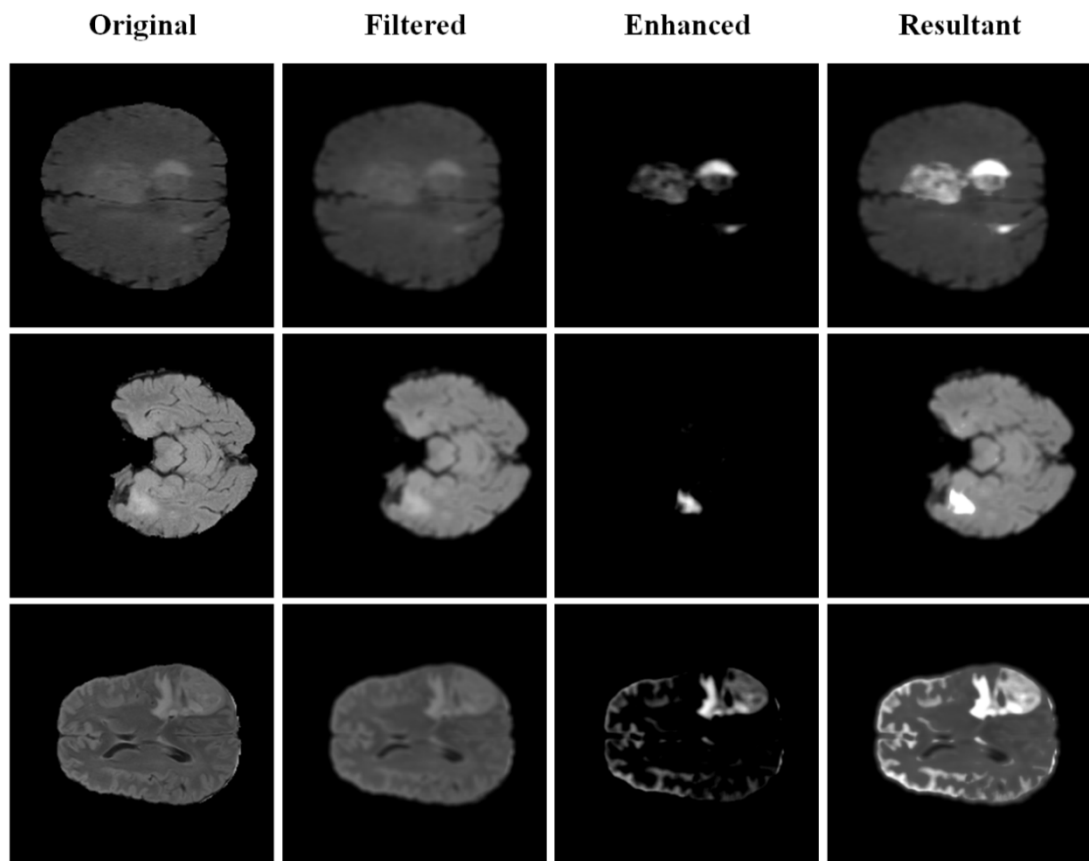
Finally, the enhanced image is added to the initially filtered one, and the resultant image  $O_R$  is obtained to be fed to the traditional U-Net architecture, as shown in Equation 15.

$$O_R = I_f + O_i \quad (15)$$

Where  $I_f$  denotes the filtered image and  $O_i$  is defined as  $O_T$  or  $O_B$  according to Equation 10. Figure 13 demonstrates the results of the pre-processing methods on sample images.

Figure 13.

*The Results of the Pre-processing Methods on Sample Images.*

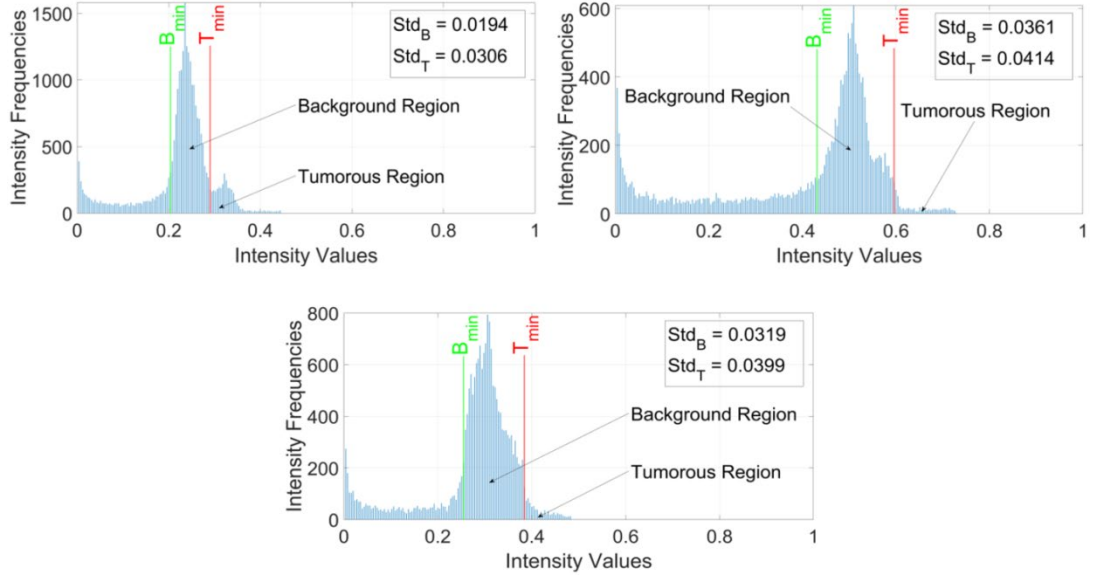


Similarly, the 4<sup>th</sup> column of Figure 13 demonstrates the resultant images; however, it is clearly seen that in some images, similar components of the brain that have close intensity values with tumorous regions are also localized and enhanced, and this makes the use of supervised segmentation methods compulsory, such as the U-Net to avoid the segmentation of irrelevant regions.

Figure 14 demonstrates the determined background and tumorous regions (with minimum values  $B_{min}$  and  $T_{min}$ ) using the proposed tumor localization method and their corresponding standard deviations on the normalized histograms of the filtered images presented in Figure 13.

Figure 14.

*Visualization of the Proposed Tumor Localization Method.*



### Evaluation Metrics

There are various metrics to evaluate the performance of the systems developed for the image segmentation tasks (Al-Antari, et al., 2018; Nai, et al., 2021). In this study, six metrics are used: accuracy, sensitivity, specificity, precision, dice score, and Jaccard index to evaluate the performance of the proposed system.

The accuracy represents the overall success rate of the system and is defined as in Equation 16.

$$Accuracy = \frac{TP + TN}{TP + FN + TN + FP} * 100 \quad (16)$$

The sensitivity (recall) measures the system's ability to segment tumorous pixels and is defined in Equation 17.

$$Sensitivity = \frac{TP}{TP + FN} * 100 \quad (17)$$

Contrary to the sensitivity, specificity shows the ability of the system to segment the non-tumorous pixels. The equation of specificity is given in Equation 18.

$$\textit{Specificity} = \frac{TN}{TN + FP} * 100 \quad (18)$$

The precision represents the ratio of the correctly classified tumorous pixels over all pixels that are classified as tumorous by the system. This led researchers to analyze the success of the system in producing true positives over all pixels assigned as tumorous. It is defined in Equation 19.

$$\textit{Precision} = \frac{TP}{TP + FP} * 100 \quad (19)$$

The dice score and Jaccard index are the most common evaluation metrics that are used to evaluate the segmentation results. They are the measurements of the common pixels between the segmented and ground truth images and are defined as in Equation 20 and 21.

$$\textit{Dice Score} = \frac{2TP}{2TP + FP + FN} \quad (20)$$

$$\textit{Jaccard Index} = \frac{TP}{TP + FP + FN} \quad (21)$$



## CHAPTER VI

### Results and Discussions

This chapter presents the experiments and their results performed to evaluate the performance of the proposed system, comparison analyses, and discussions on the advantages and limitations of the study.

#### Experimental Design

In this study, five experiments are performed to evaluate the performance of the proposed system. The training is implemented using k-fold cross-validation (Wong, 2015), where the k value is determined as five, and Adam optimizer. Each fold is evaluated using the metrics mentioned in the evaluation metrics section of the methodology. The mean values of each metric are used as the final evaluation result.

In the first experiment, the proposed system is tested on the resized (240x240) HGG images of the BRATS 2012 dataset. The training parameters are determined as 0.001, 50, and 8 for the learning rate, the number of epochs, and batch size, respectively. In the second experiment, the proposed system is tested on the resized (240x240) LGG images of the BRATS 2012 dataset using the trained network that achieved highest dice score and Jaccard index in the first experiment. In the third experiment, the proposed system is tested on the BRATS 2019 dataset without distinguishing HGG-LGG. The training parameters are determined as 0.001, 10, and 8 for the learning rate, the number of epochs, and batch size, respectively. The only difference between the third and the fourth experiments is that the proposed system is tested on the BRATS 2020 dataset. In the last experiment, the traditional U-Net's performance is tested on the original images of the BRATS 2012 HGG, BRATS 2012 LGG, and BRATS 2020 datasets without any training/testing strategy and parameter changes to prove the efficiency of the applied pre-processing methods. The reason why it is not tested on the BRATS 2019 dataset is that this experiment was performed in one of the comparative studies (Zeineldin, et al., 2020).

All experiments are performed using a computer with 32 GB of RAM, NVIDIA GeForce RTX 2080 graphics processor, and i7-8<sup>th</sup> Generation CPU on Windows 10 OS.

## Results

In the first experiment, the close results are obtained in each fold when the accuracy, specificity, dice score, and Jaccard index metrics are considered. There are fluctuations in the fold results for the sensitivity since the minimum sensitivity is obtained in Fold 3, with approximately a 5% decrease (89.47% and 94.65%, respectively). The highest dice score and Jaccard Index are obtained in Fold 4 (0.95 and 0.90, respectively). The proposed system achieved the mean accuracy, sensitivity, specificity, precision, dice score, and Jaccard index as 99.38%, 92.19%, 99.75%, 95.04%, 0.94, and 0.88, respectively. Table 1 presents the obtained results for the BRATS 2012 HGG images in detail.

Table 1.

*Evaluation Results of the BRATS 2012 HGG Images.*

Fold	Accuracy (%)	Sensitivity (%)	Specificity (%)	Precision (%)	Dice	Jaccard
1	99.32%	92.10%	99.69%	93.70%	0.93	0.87
2	99.27%	<b>94.65%</b>	99.50%	90.37%	0.92	0.86
3	99.38%	89.47%	<b>99.88%</b>	<b>97.41%</b>	0.93	0.87
4	<b>99.47%</b>	92.88%	99.82%	96.40%	<b>0.95</b>	<b>0.90</b>
5	<b>99.47%</b>	91.86%	99.87%	97.30%	0.94	<b>0.90</b>
Mean	99.38%	92.19%	99.75%	95.04%	0.94	0.88

The second experiment is aimed to demonstrate the efficiency of the proposed system in segmenting the untrained images with different characteristics. Table 2 presents the obtained results for the BRATS 2012 LGG images.

Table 2.

*Evaluation Results of the BRATS 2012 LGG Images.*

Accuracy (%)	Sensitivity (%)	Specificity (%)	Precision (%)	Dice	Jaccard
99.12%	83.27%	99.62%	87.18%	0.85	0.74

In the third experiment, consistent results are obtained when accuracy and specificity are considered. Even though a decrease is observed in the sensitivity result of Fold 2 (74.71%), stable results are obtained in general, and 83.01% mean sensitivity is achieved. Similarly, consistent precision results are obtained except for Fold 1 (87.79%), and the mean precision result of the proposed system is recorded as 92.60%. The highest dice score and Jaccard index are obtained in Fold 3 and Fold 5 with the same results (0.89 and 0.80, respectively). The proposed system achieved the mean accuracy, specificity, dice score, and Jaccard index as 99.38%, 99.82%, 0.87, and 0.78, respectively. Table 3 presents the obtained results for the BRATS 2019 dataset in detail.

Table 3.

*Evaluation Results of the BRATS 2019 Dataset.*

Fold	Accuracy (%)	Sensitivity (%)	Specificity (%)	Precision (%)	Dice	Jaccard
1	99.34%	<b>87.21%</b>	99.67%	87.79%	0.87	0.78
2	99.27%	74.71%	<b>99.92%</b>	<b>96.23%</b>	0.84	0.73
3	<b>99.44%</b>	85.34%	99.81%	92.42%	<b>0.89</b>	<b>0.80</b>
4	99.42%	82.98%	99.86%	93.83%	0.88	0.79
5	99.43%	84.82%	99.82%	92.72%	<b>0.89</b>	<b>0.80</b>
Mean	99.38%	83.01%	99.82%	92.60%	0.87	0.78

In the fourth experiment, the close results are obtained in each fold when the accuracy, specificity, dice score, and Jaccard index metrics are considered. There are fluctuations in the fold results for the sensitivity since the minimum sensitivity is obtained in Fold 5, with approximately a 7% decrease (80.61% and 87.89%, respectively). Similarly, consistent precision results are obtained except for Fold 4 (90.66%). The highest dice score and Jaccard index are obtained as 0.89 (Fold 3 and Fold 4) and 0.81 (Fold 4), respectively. The proposed system achieved the mean accuracy, sensitivity, specificity, precision, dice score, and Jaccard index as 99.40%, 83.62%, 99.83%, 92.94%, 0.88, and 0.79, respectively. Table 4 presents the obtained results for the BRATS 2020 dataset in detail.

Table 4.

*Evaluation Results of the BRATS 2020 Dataset.*

Fold	Accuracy (%)	Sensitivity (%)	Specificity (%)	Precision (%)	Dice	Jaccard
1	99.37%	80.96%	99.87%	94.17%	0.87	0.77
2	99.40%	82.16%	99.85%	93.71%	0.88	0.78
3	99.43%	86.51%	99.78%	91.17%	<b>0.89</b>	0.80
4	<b>99.45%</b>	<b>87.89%</b>	99.76%	90.66%	<b>0.89</b>	<b>0.81</b>
5	99.37%	80.61%	<b>99.88%</b>	<b>95.01%</b>	0.87	0.77
Mean	99.40%	83.62%	99.83%	92.94%	0.88	0.79

In the last experiment, the traditional U-Net architecture achieved 0.90, 0.82, 0.81, 0.85 dice scores for the BRATS 2012 HGG, BRATS 2012 LGG, BRATS 2019, and BRATS 2020 datasets, respectively and lagged behind the proposed system.

In addition to the last experiment, the proposed system and the traditional U-Net architecture are tested on the BRATS 2020 validation set to justify the superiority of the proposed system using the BRATS online evaluation platform. The proposed system and the traditional U-Net architecture achieved 0.81 and 0.77 dice scores, respectively.

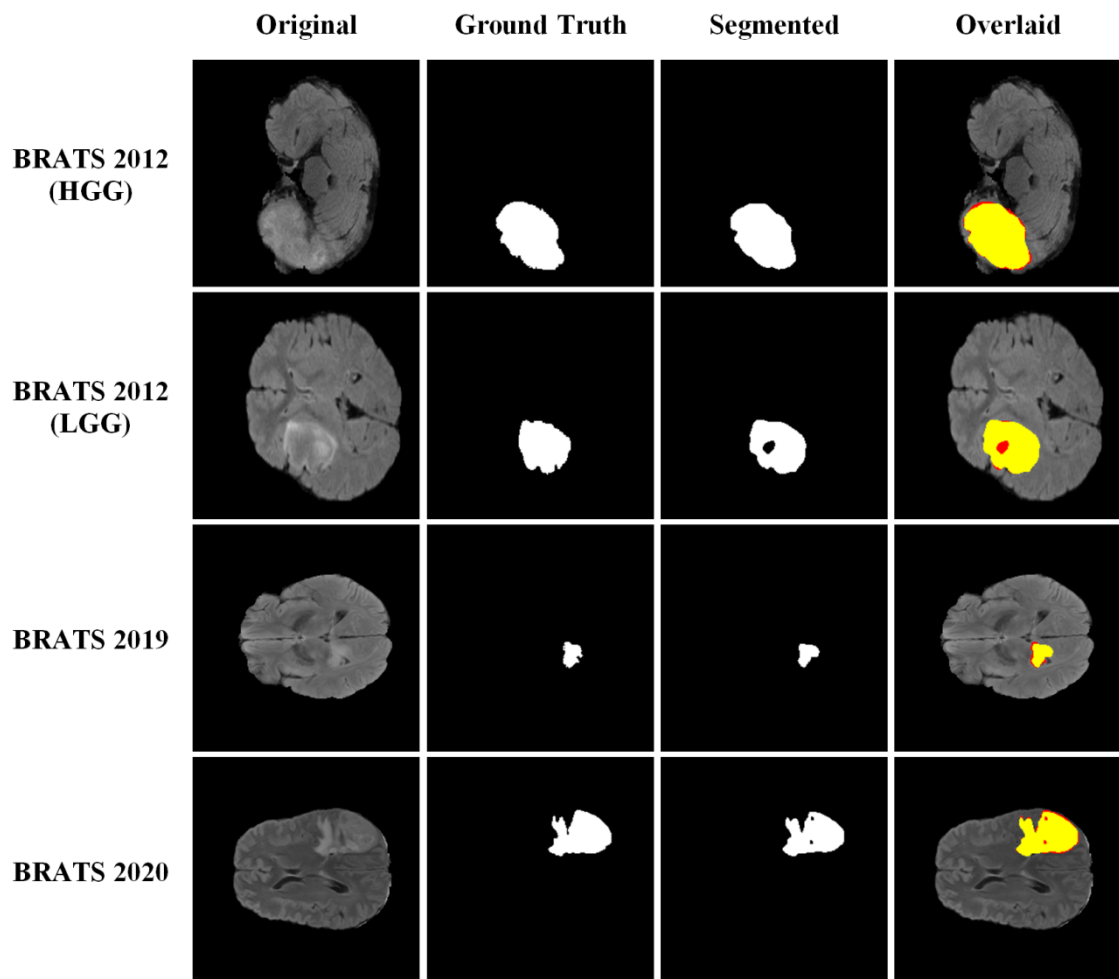
At the end of the experiments, the average tumor volume is calculated for each dataset. The volumes are obtained using the number of tumor voxels multiplied by the voxel volume (Montelius, et al., 2012) and converted to  $\text{cm}^3$  after calculating the average of all slices. Then, the correctly segmented tumor volumes are calculated and compared to the actual values to observe the agreement.

The agreement between the tumor volume extracted on the ground truth images and the outputs of the proposed system are calculated as 92.22%, 83.48%, 83.01%, and 83.57% for the BRATS 2012 HGG, BRATS 2012 LGG, BRATS 2019, and BRATS 2020 datasets, respectively.

Figure 15 demonstrates the segmentation results, including a sample for each considered dataset.

Figure 15.

*Sample Segmentation Results of the Proposed System.*



Where red and yellow regions in the overlaid images represent the ground truth and segmented tumor by the proposed system, respectively.

### *Comparisons*

The proposed system is compared with the recent studies that focused on the complete brain tumor segmentation task. Tables 5, 6, and 7 show the comparison results of the proposed system for the BRATS 2012 (HGG-LGG), BRATS 2019, and BRATS 2020 datasets, respectively.

Table 5.

*Comparison Results of the Proposed System on BRATS 2012 Dataset.*

Study	Tumor Type	Method	Dice
-------	------------	--------	------

Table 5 (Continued).

-	HGG	Traditional U-Net	0.90
	LGG (untrained)		0.82
(Eltayeb, et al., 2019)	HGG	K-means Clustering with CH cluster validity index	0.89
	LGG		0.84
(Rehman, et al., 2020)	HGG	LOOCV and RF	0.88
	LGG		0.81
(Chithra & Dheepa, 2020)	HGG	CNN architecture based on Di-phase midway	0.84
	LGG		<b>0.85</b>
Proposed	HGG	Tumor localization and enhancement methods + traditional U-Net	<b>0.94</b>
	LGG (untrained)		<b>0.85</b>

Table 6.

*Comparison Results of the Proposed System on BRATS 2019 Dataset.*

Study	Tumor Type	Method	Dice
(Zeineldin, et al., 2020)	Combined	Traditional U-Net	0.81
	Combined	Combination of modified U-Net and Xception architectures	0.84
(Sohail, et al., 2021)	Combined	3D U-Net	0.78
Proposed	Combined	Tumor localization and enhancement methods + traditional U-Net	<b>0.87</b>

Table 7.

*Comparison Results of the Proposed System on BRATS 2020 Dataset.*

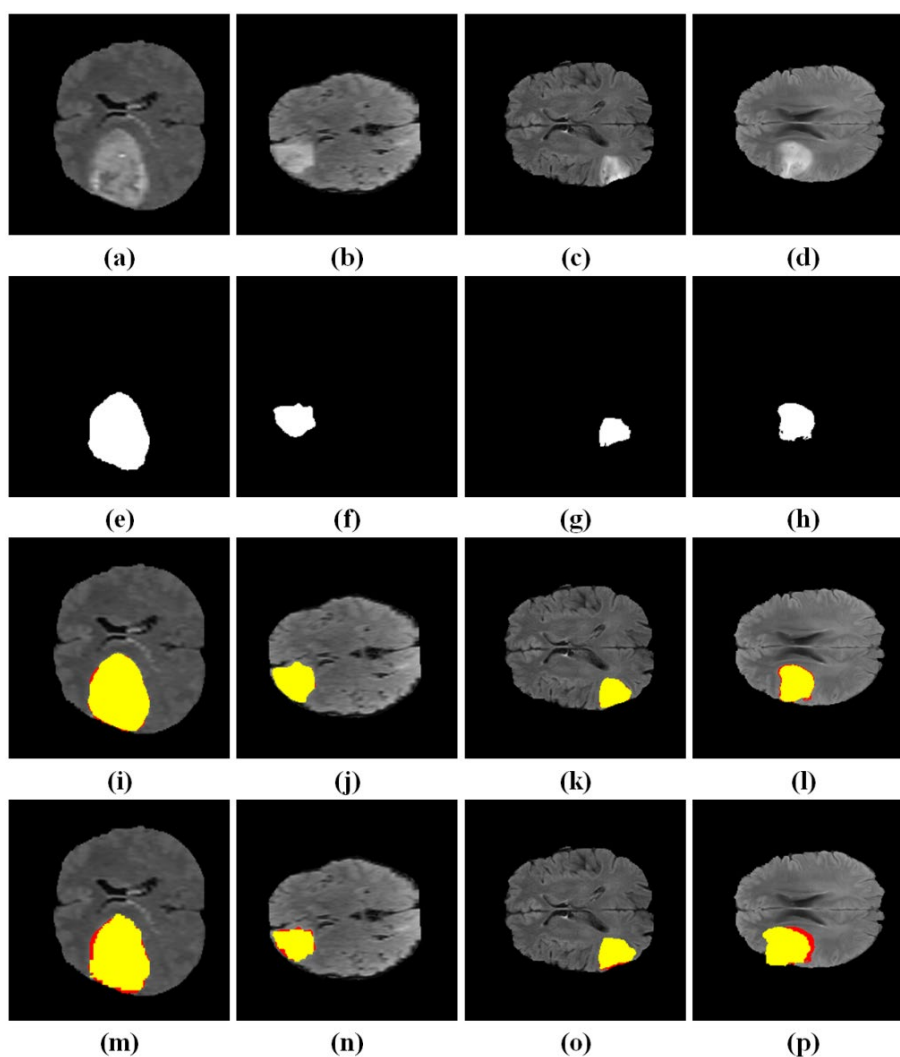
Study	Tumor Type	Method	Dice
-	Combined	Traditional U-Net	0.85
(Sohail, et al., 2021)	Combined	3D U-Net	0.72

Table 7 (Continued).

(Zhao, et al., 2021)	Combined	MVP U-Net	0.80
(Ballestar & Vilaplana, 2021)	Combined	V-Net	0.87
Proposed	Combined	Tumor localization and enhancement methods + traditional U-Net	<b>0.88</b>

Figure 16 shows the visualization of the comparative segmentation results. It is clear that the all of the proposed methods in the literature are capable of segmenting complete brain tumors; however, the details localized and enhanced by our proposed methods create differences within other methods and the produced results.

Figure 16.

*Comparative Segmentation Results.*

Where (a)-(d) original images for the BRATS 2012 HGG, BRATS 2012 LGG, BRATS 2019, and BRATS 2020 datasets, respectively; (e)-(h) corresponding ground truth images, (i)-(l) overlaid outputs of the proposed system, (m)-(n) (Eltayeb, et al., 2019), (o) (Zeineldin, et al., 2020), and (p) (Ballestar & Vilaplana, 2021).

## Discussions

The lack of distinct tumors in MRI images requires enhancing these regions to provide more accurate segmentation. However, the enhancement of the tumor region initially requires effective localization to apply enhancement only to the region of interest.

The localization of the tumors according to the basic characteristics of the images using a non-parametric localization method enabled us to apply the proposed enhancement method to increase the visual appearances of indistinct tumors. Similarly, the proposed localization and enhancement methods minimize segmentation errors for the distinct tumors that occurred in high-contrast images by adjusting the pixel values similar to the background within the tumorous region. Therefore, indistinct tumorous regions or pixels are clarified, and the background regions are preserved with low computation cost (average processing time / image = 0.0028 sec.).

Due to the non-parametric and automated procedure of the proposed methods, the computational cost is minimized by preventing the selection of any parameters for the images. This also provided more distinguishable tumorous regions and informative features to the traditional U-Net architecture to extract features more efficiently and perform segmentation with highly accurate results. The supervised learning and feature extraction nature of the deep learning architectures focuses on the regions provided in the ground truths to extract the relevant features and obtain the ability to segment untrained data.

Applied pre-processing methods yielded the deep learning architecture to mainly focus on the enhanced and visually improved tumorous regions by eliminating and not considering irrelevant components. This increased the segmentation results of the traditional U-Net architecture by 0.04, 0.03, 0.06, and 0.03 for the BRATS 2012 HGG, BRATS 2012 LGG, BRATS 2019, and BRATS 2020 datasets, respectively.



In addition, the validation set results obtained from the BRATS online evaluation platform prove that the applied pre-processing methods increased the traditional U-Net's segmentation ability by a 0.04 dice score.

The obtained results showed that the low-cost pre-processing of images significantly increases the segmentation abilities of deep learning architectures without modifying the internal architecture. On the other hand, datasets are trained without any data augmentation technique and minimize the computational time for the U-Net architecture training.

The limitation of the proposed system is determined on the images consist of multiple indistinct tumorous regions with a few pixels. This is based on the assumption that the tumor is a single region; however, the methods could be modified to detect multiple regions to avoid this limitation in the future. Another limitation of the study is the consideration of the FLAIR images only for complete tumor segmentation and not testing the proposed methods with other modalities for segmenting tumors as multi-class. Our future work will focus on this subject.

## CHAPTER VII

### Conclusion

In this study, the proposed non-parametric tumor localization and enhancement methods are combined with the traditional U-Net architecture and proposed as a complete brain tumor segmentation system. The proposed system is tested on three benchmark datasets named BRATS 2012 (HGG and untrained LGG), BRATS 2019, and BRATS 2020 and the superior segmentation performance is obtained in segmenting complete brain tumors by achieving 0.94, 0.85, 0.87, and 0.88 dice scores, respectively.

In addition, in the experiments performed to compare the performances of the proposed system and the traditional U-Net architecture, the proposed system is reported as superior.

The results showed that the effective localization and enhancement of tumorous regions yield the deep learning architectures to learn features more effectively and segment the trained or untrained datasets accurately without requiring data augmentation techniques and modifications.

The future work will include improving the proposed system to segment sub-classes of brain tumors named core and enhancing tumors after performing complete tumor segmentation.

## References

- Al-Antari, M. A., Al-Masni, M. A., Choi, M. T., Han, S. M., & Kim, T. S. (2018). A fully integrated computer-aided diagnosis system for digital X-ray mammograms via deep learning detection, segmentation, and classification. *International journal of medical informatics*, *117*, 44-54. <https://doi.org/10.1016/j.ijmedinf.2018.06.003>
- Allen, M. (Ed.). (2017). *The SAGE encyclopedia of communication research methods*. Sage Publications
- Amin, J., Sharif, M., Raza, M., Saba, T., & Anjum, M. A. (2019). Brain tumor detection using statistical and machine learning method. *Computer methods and programs in biomedicine*, *177*, 69-79. <https://doi.org/10.1016/j.cmpb.2019.05.015>
- Anitha, V., & Murugavalli, S. J. I. C. V. (2016). Brain tumour classification using two-tier classifier with adaptive segmentation technique. *IET computer vision*, *10*(1), 9-17. <http://doi.org/10.1049/iet-cvi.2014.0193>
- Badrinarayanan, V., Kendall, A., & Cipolla, R. (2017). SegNet: A deep convolutional encoder-decoder architecture for image segmentation. *IEEE transactions on pattern analysis and machine intelligence*, *39*(12), 2481-2495. <https://doi.org/10.1109/TPAMI.2016.2644615>
- Bakas, S., Akbari, H., Sotiras, A., Bilello, M., Rozycki, M., Kirby, J. S., ... & Davatzikos, C. (2017). Advancing the cancer genome atlas glioma MRI collections with expert segmentation labels and radiomic features. *Nature Scientific data*, *4*(1), 1-13. <https://doi.org/10.1038/sdata.2017.117>
- Bakas, S., Reyes, M., Jakab, A., Bauer, S., Rempfler, M., Crimi, A., ... & Jambawalikar, S. R. (2018). Identifying the best machine learning algorithms for brain tumor segmentation, progression assessment, and overall survival prediction in the BRATS challenge. *arXiv preprint arXiv:1811.02629*.
- Ballestar, L. M., & Vilaplana, V. (2021). MRI brain tumor segmentation and uncertainty estimation using 3D-UNet architectures. In: Crimi A., Bakas S. (eds) *Brainlesion: Glioma, Multiple Sclerosis, Stroke and Traumatic Brain Injuries. BrainLes 2020. Lecture Notes in Computer Science*, vol 12658, (pp. 376-390) Springer, Cham. [https://doi.org/10.1007/978-3-030-72084-1\\_34](https://doi.org/10.1007/978-3-030-72084-1_34)

- Burger, W., & Burge, M. J. (2016). *Digital image processing: an algorithmic introduction using Java*. Springer-Verlag, London.
- Chithra, P. L., & Dheepa, G. (2020). Di-phase midway convolution and deconvolution network for brain tumor segmentation in MRI images. *International Journal of Imaging Systems and Technology*, 30(3), 674-686. <https://doi.org/10.1002/ima.22407>
- Currie, S., Hoggard, N., Craven, I. J., Hadjivassiliou, M., & Wilkinson, I. D. (2013). Understanding MRI: basic MR physics for physicians. *Postgraduate medical journal*, 89(1050), 209-223. <http://doi.org/10.1136/postgradmedj-2012-131342>
- Eltayeb, E. N., Salem, N. M., & Al-Atabany, W. (2019). Automated brain tumor segmentation from multi-slices FLAIR MRI images. *Bio-medical materials and engineering*, 30(4), 449-462. <https://doi.org/10.3233/BME-191066>
- Gonzalez, R. C., & Woods, R. E. (2002). *Digital Image Processing*. Beijing: Publishing house of electronics industry.
- Gonzalez, R. C., & Woods, R. E. (2008). *Digital image processing*. Upper Saddle River, New Jersey, NJ: Pearson Prentice Hall.
- Hussain, A. J., Al-Fayadh, A., & Radi, N. (2018). Image compression techniques: A survey in lossless and lossy algorithms. *Neurocomputing*, 300, 44-69. <https://doi.org/10.1016/j.neucom.2018.02.094>
- Ilhan, U., & Ilhan, A. (2017). Brain tumor segmentation based on a new threshold approach. *Procedia computer science*, 120, 580-587. <https://doi.org/10.1016/j.procs.2017.11.282>
- Kalaiselvi, T., Kumarashankar, P., & Sriramakrishnan, P. (2020). Three-phase automatic brain tumor diagnosis system using patches based updated run length region growing technique. *Journal of digital imaging*, 33(2), 465-479. <https://doi.org/10.1007/s10278-019-00276-2>
- Kapoor, K., & Kaushik, H. (2018). Review Paper on Various Image Compression Techniques. *International Journal of All Research Education and Scientific Methods*, 6(7), 30-35.
- Karthik, R., Gupta, U., Jha, A., Rajalakshmi, R., & Menaka, R. (2019). A deep supervised approach for ischemic lesion segmentation from multimodal MRI using Fully Convolutional Network. *Applied Soft Computing*, 84, 105685. <https://doi.org/10.1016/j.asoc.2019.105685>

- Kermi, A., Andjouh, K., & Zidane, F. (2018). Fully automated brain tumour segmentation system in 3D-MRI using symmetry analysis of brain and level sets. *IET Image Processing*, *12*(11), 1964-1971. <https://doi.org/10.1049/iet-ipr.2017.1124>
- Khalil, H. A., Darwish, S., Ibrahim, Y. M., & Hassan, O. F. (2020). 3D-MRI brain tumor detection model using modified version of level set segmentation based on dragonfly algorithm. *Symmetry*, *12*(8), 1256. <https://doi.org/10.3390/sym12081256>
- LeCun, Y., Bengio, Y., & Hinton, G. (2015). Deep learning. *nature*, *521*(7553), 436-444. <https://doi.org/10.1038/nature14539>
- Li, X., Guo, Y., Jiang, F., Xu, L., Shen, F., Jin, Z., & Wang, Y. (2020). Multi-task refined boundary-supervision U-Net (MRBSU-Net) for gastrointestinal stromal tumor segmentation in endoscopic ultrasound (EUS) images. *IEEE Access*, *8*, 5805-5816. <https://doi.org/10.1109/ACCESS.2019.2963472>
- Menze, B. H., Jakab, A., Bauer, S., Kalpathy-Cramer, J., Farahani, K., Kirby, J., ... & Van Leemput, K. (2015). The multimodal brain tumor image segmentation benchmark (BRATS). *IEEE transactions on medical imaging*, *34*(10), 1993-2024. <https://doi.org/10.1109/TMI.2014.2377694>
- Montelius, M., Ljungberg, M., Horn, M., & Forssell-Aronsson, E. (2012). Tumour size measurement in a mouse model using high resolution MRI. *BMC medical imaging*, *12*(1), 1-7. <https://doi.org/10.1186/1471-2342-12-12>
- Nai, Y. H., Teo, B. W., Tan, N. L., O'Doherty, S., Stephenson, M. C., Thian, Y. L., ... & Reilhac, A. (2021). Comparison of metrics for the evaluation of medical segmentations using prostate MRI dataset. *Computers in Biology and Medicine*, *134*, 104497. <https://doi.org/10.1016/j.compbiomed.2021>
- Pang, Y., Sun, M., Jiang, X., & Li, X. (2017). Convolution in convolution for network in network. *IEEE transactions on neural networks and learning systems*, *29*(5), 1587-1597. <https://doi.org/10.1109/TNNLS.2017.2676130>
- Pereira, S., Pinto, A., Alves, V., & Silva, C. A. (2016). Brain tumor segmentation using convolutional neural networks in MRI images. *IEEE transactions on medical imaging*, *35*(5), 1240-1251. <https://doi.org/10.1109/TMI.2016.2538465>
- Rehman, Z. U., Naqvi, S. S., Khan, T. M., Khan, M. A., & Bashir, T. (2019). Fully automated multi-parametric brain tumour segmentation using superpixel

- based classification. *Expert systems with applications*, 118, 598-613. <https://doi.org/10.1016/j.eswa.2018.10.040>
- Rehman, Z. U., Zia, M. S., Bojja, G. R., Yaqub, M., Jinchao, F., & Arshid, K. (2020). Texture based localization of a brain tumor from MR-images by using a machine learning approach. *Medical hypotheses*, 141, 109705. <https://doi.org/10.1016/j.mehy.2020.109705>
- Ronneberger O., Fischer P., Brox T. (2015) U-Net: Convolutional Networks for Biomedical Image Segmentation. In: Navab N., Hornegger J., Wells W., Frangi A. (eds) *Medical Image Computing and Computer-Assisted Intervention MICCAI 2015. Lecture Notes in Computer Science*, vol 9351. (pp. 234-241) Springer, Cham. [https://doi.org/10.1007/978-3-319-24574-4\\_28](https://doi.org/10.1007/978-3-319-24574-4_28)
- Rundo, L., Han, C., Nagano, Y., Zhang, J., Hataya, R., Militello, C., ... & Cazzaniga, P. (2019). USE-Net: Incorporating Squeeze-and-Excitation blocks into U-Net for prostate zonal segmentation of multi-institutional MRI datasets. *Neurocomputing*, 365, 31-43. <https://doi.org/10.1016/j.neucom.2019.07.006>
- Sohail, N., Anwar, S. M., Majeed, F., Sanin, C., & Szczerbicki, E. (2021). Smart Approach for Glioma Segmentation in Magnetic Resonance Imaging using Modified Convolutional Network Architecture (U-NET). *Cybernetics and Systems*, 52(5), 445-460. <https://doi.org/10.1080/01969722.2020.1871231>
- Soltaninejad, M., Yang, G., Lambrou, T., Allinson, N., Jones, T. L., Barrick, T. R., ... & Ye, X. (2017). Automated brain tumour detection and segmentation using superpixel-based extremely randomized trees in FLAIR MRI. *International journal of computer assisted radiology and surgery*, 12(2), 183-203. <https://doi.org/10.1007/s11548-016-1483-3>
- Song, L. I., Geoffrey, K. F., & Kaijian, H. E. (2020). Bottleneck feature supervised U-Net for pixel-wise liver and tumor segmentation. *Expert Systems with Applications*, 145, 113131. <https://doi.org/10.1016/j.eswa.2019.113131>
- Tong, G., Li, Y., Chen, H., Zhang, Q., & Jiang, H. (2018). Improved U-NET network for pulmonary nodules segmentation. *Optik*, 174, 460-469. <https://doi.org/10.1016/j.ijleo.2018.08.086>
- Wang, J., Lu, J., Qin, G., Shen, L., Sun, Y., Ying, H., ... & Hu, W. (2018). A deep learning-based autosegmentation of rectal tumors in MR images. *Medical physics*, 45(6), 2560-2564. <https://doi.org/10.1002/mp.12918>

- Wong, T. T. (2015). Performance evaluation of classification algorithms by k-fold and leave-one-out cross validation. *Pattern Recognition*, 48(9), 2839-2846. <https://doi.org/10.1016/j.patcog.2015.03.009>
- Wu, W., Li, D., Du, J., Gao, X., Gu, W., Zhao, F., ... & Yan, H. (2020). An intelligent diagnosis method of brain MRI tumor segmentation using deep convolutional neural network and SVM algorithm. *Computational and Mathematical Methods in Medicine*, 2020, 6789306. <https://doi.org/10.1155/2020/6789306>
- Yamashita, R., Nishio, M., Do, R. K. G., & Togashi, K. (2018). Convolutional neural networks: an overview and application in radiology. *Insights into imaging*, 9(4), 611-629. <https://doi.org/10.1007/s13244-018-0639-9>
- Zeineldin, R. A., Karar, M. E., Coburger, J., Wirtz, C. R., & Burgert, O. (2020). DeepSeg: deep neural network framework for automatic brain tumor segmentation using magnetic resonance FLAIR images. *International journal of computer assisted radiology and surgery*, 15(6), 909-920. <https://doi.org/10.1007/s11548-020-02186-z>
- Zhao, C., Zhao, Z., Zeng, Q., & Feng, Y. (2021). MVP U-Net: Multi-View Pointwise U-Net for Brain Tumor Segmentation. In: Crimi A., Bakas S. (eds) *Brainlesion: Glioma, Multiple Sclerosis, Stroke and Traumatic Brain Injuries. BrainLes 2020. Lecture Notes in Computer Science*, vol 12659, (pp. 93-103). Springer, Cham. [https://doi.org/10.1007/978-3-030-72087-2\\_9](https://doi.org/10.1007/978-3-030-72087-2_9)

**APPENDICES****Appendix A****Ethical Approval Document**

There is no ethical approval document that can be presented.

Prof. Dr. Rahib ABIYEV  
Supervisor



## Appendix B

### Curriculum Vitae

#### Personal Information

Surname, Name: İlhan, Ahmet

Date of Birth: 31 December 1992

Place of Birth: Nicosia, Cyprus

Table B1.

*Education.*

Degree	Department/Program	University	Year of Graduation
B.Sc.	Computer Engineering	Near East University	2014
M.Sc.	Computer Engineering	Near East University	2017

Table B2.

*Work Experience.*

Title	Place	Year
Research Assistant	NEU, Faculty of Engineering, Department of Computer Engineering	2014-2017
Lecturer	NEU, Faculty of Engineering, Department of Computer Engineering	2017-present

#### Foreign Languages

Fluent spoken and written English.

#### Publications in International Journals and Conferences

Ilhan, A., Sekeroglu, B., & Abiyev, R. (2022). Brain tumor segmentation in MRI images using nonparametric localization and enhancement methods with U-net. *International Journal of Computer Assisted Radiology and Surgery*, 1-12. <https://doi.org/10.1007/s11548-022-02566-7>

Özçil, İ. E., Esenyel, İ., & İlhan, A. (2022). A Fuzzy Approach Analysis of Halloumi Cheese in N. Cyprus. *Food Analytical Methods*, 15(1), 10-15. <https://doi.org/10.1007/s12161-021-02075-4>

Ilhan, U., İlhan, A., Uyar, K., & Iseri, E. I. (2021, October). Classification of Osmancik and Cammeo Rice Varieties using Deep Neural Networks. In *2021*

*5th International Symposium on Multidisciplinary Studies and Innovative Technologies (ISMSIT)* (pp. 587-590). IEEE.

<https://doi.org/10.1109/ISMSIT52890.2021.9604606>

Sekeroglu, B., Abiyev, R., İlhan, A., Arslan, M., & Idoko, J. B. (2021). Systematic Literature Review on Machine Learning and Student Performance Prediction: Critical Gaps and Possible Remedies. *Applied Sciences*, *11*(22), 10907.

<https://doi.org/10.3390/app112210907>

Işın, A., Kaba, Ş., & İlhan, A. (2020, August). A Review on Recent Deep Learning-Based Computer-Aided Systems for Breast Cancer Diagnosis. In *International Conference on Theory and Applications of Fuzzy Systems and Soft Computing* (pp. 289-296). Springer, Cham. [https://doi.org/10.1007/978-3-030-64058-3\\_36](https://doi.org/10.1007/978-3-030-64058-3_36)

Uyar, K., İlhan, U., İlhan, A., & Iseri, E. I. (2020, April). Breast cancer prediction using neuro-fuzzy systems. In *2020 7th International Conference on Electrical and Electronics Engineering (ICEEE)* (pp. 328-332). IEEE.

<https://doi.org/10.1109/ICEEE49618.2020.9102476>

Abiyev, R., Arslan, M., Bush Idoko, J., Sekeroglu, B., & İlhan, A. (2020). Identification of epileptic EEG signals using convolutional neural networks. *Applied Sciences*, *10*(12), 4089. <https://doi.org/10.3390/app10124089>

Uyar, K., İlhan, U., Iseri, E. I., & İlhan, A. (2019, October). Forecasting measles cases in Ethiopia using neuro-fuzzy systems. In *2019 3rd international symposium on multidisciplinary studies and innovative technologies (ISMSIT)* (pp. 1-5). IEEE. <https://doi.org/10.1109/ISMSIT.2019.8932882>

İlhan, A., Kaba, Ş., & Kneebone, E. (2019, April). Vertebral Body Compression Fracture Detection. In *Science and Information Conference* (pp. 361-368). Springer, Cham. [https://doi.org/10.1007/978-3-030-17795-9\\_26](https://doi.org/10.1007/978-3-030-17795-9_26)

İlhan, U., & İlhan, A. (2017). Brain tumor segmentation based on a new threshold approach. *Procedia computer science*, *120*, 580-587.

<https://doi.org/10.1016/j.procs.2017.11.282>

Uyar, K., & İlhan, A. (2017). Diagnosis of heart disease using genetic algorithm based trained recurrent fuzzy neural networks. *Procedia computer science*, *120*, 588-593. <https://doi.org/10.1016/j.procs.2017.11.283>

- Dimililer, K., & İlhan, A. (2016). Effect of image enhancement on MRI brain images with neural networks. *Procedia Computer Science*, 102, 39-44. <https://doi.org/10.1016/j.procs.2016.09.367>
- Uyar, K., & İlhan, A. (2016). Long term dry cargo freight rates forecasting by using recurrent fuzzy neural networks. *Procedia Computer Science*, 102, 642-647. <https://doi.org/10.1016/j.procs.2016.09.455>










## Appendix C

### Similarity Report

#### Ph.D. Thesis

INBOX | NOW VIEWING: NEW PAPERS ▼

Submit File

<input type="checkbox"/>	AUTHOR	TITLE	SIMILARITY
<input type="checkbox"/>	Ahmet İhan	Abstract	0% 
<input type="checkbox"/>	Ahmet İhan	Chapter 7 (Conclusion)	0% 
<input type="checkbox"/>	Ahmet İhan	Chapter 1 (Introduction)	2% 
<input type="checkbox"/>	Ahmet İhan	Chapter 3 (Digital Image Processing)	4% 
<input type="checkbox"/>	Ahmet İhan	Chapter 6 (Results and Discussions)	4% 
<input type="checkbox"/>	Ahmet İhan	Chapter 5 (Methodology)	5% 
<input type="checkbox"/>	Ahmet İhan	All Chapters	9% 
<input type="checkbox"/>	Ahmet İhan	Chapter 2 (Literature Review)	10% 
<input type="checkbox"/>	Ahmet İhan	Chapter 4 (Deep Learning and CNN)	12% 

Prof. Dr. Rahib ABİYEYEV  
Supervisor

## Appendix D

### Dataset Description

Table D1.

*Dataset Description.*

Dataset	Tumor Type	# Patients	# 2D Tumorous Axial FLAIR Images	# 2D Non-Tumorous Axial FLAIR Images
BRATS 2012	HGG	20	1,363	2,362
	LGG	10	485	1,423
BRATS 2019	HGG	259	17,224	22,921
	LGG	76	4,926	6,854
BRATS 2020	Combined	369	24,422	32,773